



Key Points:

- Study examines leaky barriers of cylindrical logs with inclined upstream and downstream designs for flood management
- Barrier layout affects flow dynamics, turbulence, and risk of sediment mobilization
- Upstream-inclined designs show enhanced flood management performance

Supporting Information:

Supporting Information may be found in the online version of this article.

Correspondence to:

P. Ouro,
pablo.ouro@manchester.ac.uk

Citation:

Alzabari, F., Wilson, C. A. M. E., & Ouro, P. (2024). Hydrodynamics of in-stream leaky barriers for natural flood management. *Water Resources Research*, 60, e2024WR038117. <https://doi.org/10.1029/2024WR038117>

Received 11 JUL 2024

Accepted 19 NOV 2024

Author Contributions:

Conceptualization: Fawaz Alzabari, Catherine A. M. E. Wilson, Pablo Ouro
Formal analysis: Fawaz Alzabari, Catherine A. M. E. Wilson, Pablo Ouro
Investigation: Fawaz Alzabari, Catherine A. M. E. Wilson
Methodology: Fawaz Alzabari, Catherine A. M. E. Wilson, Pablo Ouro
Project administration: Catherine A. M. E. Wilson, Pablo Ouro
Software: Fawaz Alzabari
Supervision: Catherine A. M. E. Wilson, Pablo Ouro
Validation: Fawaz Alzabari
Visualization: Fawaz Alzabari
Writing – original draft: Fawaz Alzabari
Writing – review & editing: Fawaz Alzabari, Catherine A. M. E. Wilson, Pablo Ouro

Fawaz Alzabari^{1,2} , Catherine A. M. E. Wilson¹ , and Pablo Ouro³ 

¹Hydro-Environmental Research Center, School of Engineering, Cardiff University, Cardiff, UK, ²Civil Engineering Department, College of Engineering, Najran University, Najran, Saudi Arabia, ³School of Engineering, University of Manchester, Manchester, UK

Abstract Leaky barriers are in-stream natural flood management solutions designed for peak flow attenuation, whose effectiveness is dependent on their design. Flow around leaky barriers (LB) composed of three cylindrical logs were investigated using large-eddy simulation. The main LB configuration considered vertically aligned logs, with other layouts inclined at 15°, 30°, and 45° in the upstream and downstream directions. Results reveal that the frontal projected blockage area of the LB leads to an increase in the upstream flow depth, with momentum being redirected toward the bottom gap, creating a primary wall-jet, whose peak velocity and coherence varied depending on LB design, however, attained a similar decay downstream. The porous LBs allowed for distinct internal flow paths that generated secondary jets, either diverting momentum upwards or downwards depending on the direction of the barrier inclination, impacting main flow features and turbulent characteristics. Turbulent kinetic energy and vertical Reynolds shear stress decreased when the barrier was inclined downstream. In the upstream inclination cases, these showed no significant variation, with magnitudes similar to those in the vertical configuration. Bed shear stress decreased with increasing barrier angle, reducing the risk of local scour and sediment mobilization. The vertical LB achieves the maximum backwater rise at the expense of promoting larger sediment bed mobilization. Structural loads on the logs vary with LB inclination, with drag forces decreasing as barrier angles increase. Hydrodynamic findings, evaluated through five design criteria, show that upstream-inclined designs, particularly with large barrier angles, exhibit improved relative performance compared to other designs.

1. Introduction

Extreme weather events, such as flash floods are natural disasters of increasing frequency and have demanded solutions from the scientific community, governments, industries, and risk management entities. In response, the Intergovernmental Panel on Climate Change and Paris Agreement participants have urged for considerable investment in infrastructure to ensure future water security (Fischedick et al., 2014). The Water Criteria of the Climate Bonds Standard advocates for nature-based solutions (NBS), such as instream leaky wood barriers, to improve catchment resilience and decrease dependency on hard engineering (Burgess-Gamble et al., 2017; Dadson et al., 2017). NBS for flood management is also referred to as Natural Flood Management (NFM) in the UK (Dadson et al., 2017; Lane, 2017) and Working with Natural Processes (WWNP) following the 2007 UK summer floods (Pitt, 2008); internationally, these methods are known as nature-based approaches or engineering with nature (Bridges et al., 2018).

Leaky barriers are structures inspired by natural features such as beaver dams and large woody debris in watercourses (Dadson et al., 2017; Wohl, 2013). These barriers can either mimic natural features or have a more engineered appearance. Engineered leaky barriers, which are typically constructed from large wood pieces (defined as circular logs with a diameter ≥ 0.1 m (Wohl & Jaeger, 2009)), have gained popularity due to their multiple benefits. These benefits include flood mitigation, ecological habitat enhancement, and potential local sediment redistribution (Bouwes et al., 2016; Dodd et al., 2016; Schalko et al., 2019). This latter effect is particularly beneficial in modified rivers that have lost their natural cross-sectional profile due to anthropological activities, as they supply sediment to the floodplain. However, limited data on their hydraulic performance and design guidance poses numerous challenges to their implementation (Burgess-Gamble et al., 2017). Engineered leaky barriers also represent a simplification of natural structures with uniform elements that enable an easier manufacturing and deployment. Natural design such as beaver dams and large woody debris jams consist of irregularly shaped logs and branches of varying sizes and porosity, which are difficult to represent in engineering

© 2024. The Author(s).

This is an open access article under the terms of the [Creative Commons Attribution License](https://creativecommons.org/licenses/by/4.0/), which permits use, distribution and reproduction in any medium, provided the original work is properly cited.

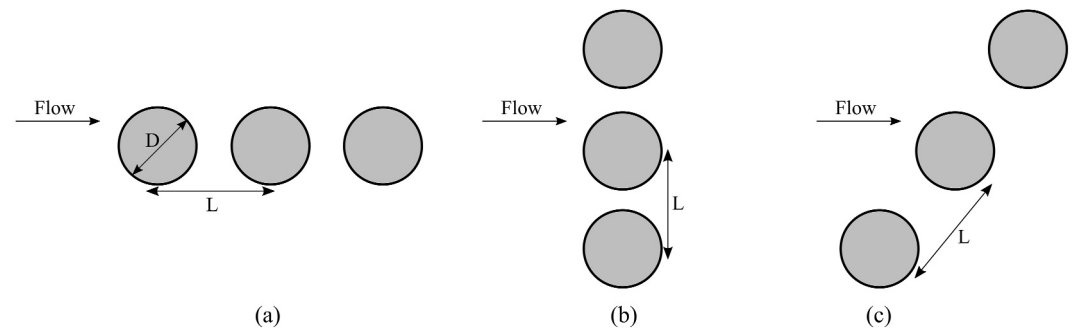


Figure 1. Side view of three cylindrical leaky barrier configuration for (a) in-line, (b) side-by-side and (c) staggered arrangements.

projects for natural flood management and whose hydrodynamics are harder to parametrize. Evaluation of the effectiveness of leaky barriers is still advancing, with few studies attempting to study the hydrodynamic flow field, their impacts on sediment transport, their water storage potential as well as how design variations impact their function (Altmann et al., 2024; Muhawenimana et al., 2021, 2023; Müller et al., 2022).

Hydrodynamics of flow around two cylinders has been extensively studied (Chen et al., 2020; Griffith et al., 2017), yet investigations into the flow around three circular cylinders, especially in very shallow free-surface flows, have received less attention. Figure 1 illustrates possible configurations of three-cylinder LB, which include in-line, side-by-side, and staggered configurations. When several cylinders are in close proximity, their mechanical response can be significantly different compared to when they are isolated. The extent of this influence depends largely on the distance between the cylinders, leading to potential interactions between boundary layers or free shear layers. Zdravkovich (1977) introduced a classification of two-cylinder flow interference in various arrangements, which includes proximity interference, wake interference, and combined interference.

For the flow around two horizontal cylinders in line arrangements, the spacing ratio L/D , where L is the center-to-center spacing of the cylinders and D is the cylinder diameter, determines the occurrence of three different flow regimes, namely extended, reattachment, and co-shedding flows (Alam, 2014; Sumner, 2010). The extended-body flow is observed when $L/D < 1.2-1.8$, where the cylinders are close enough that the flow in the gap between them becomes stagnant due to the overshooting of free shear layers from the upstream cylinder over the downstream one. In the reattachment flow regime ($1.2-1.8 < L/D < 3.4-3.8$), the shear layers reattach on the downstream cylinder, leading to a quasi-steady flow in the gap. The co-shedding flow regime occurs when $L/D > 3.4-3.8$, where the shear layers alternate in rolling up and down between the cylinders, resulting in significantly unsteady flow in the gap. The influence of the downstream cylinder on the upstream one is only noticeable for L/D ratios below 5.0; however, the upstream cylinder exhibits a significant influence on the flow around the downstream cylinder, even at larger L/D ratios (Papaioannou et al., 2006).

In the side-by-side configuration of two cylinders, the phenomenon of proximity interference occurs when the cylinders are located in close proximity to each other. Sumner (2010) identified five distinct flow patterns that occur in this configuration. For L/D values smaller than 1.1–1.2, no gap flow exists between the cylinders, and vortices are shed alternately from the free-stream sides of the cylinders, causing them to behave like a single bluff body (Alam et al., 2003). For intermediate L/D values ($1.1-1.2 < L/D < 2.0-2.2$), two flow patterns, namely the deflected flow pattern and the flip-flopping pattern, appear intermittently. The flip-flopping pattern exhibits different characteristics in low-Reynolds number (Re) laminar flow and high-Re turbulent flow.

For the flow around two staggered circular cylinders, Alam and Meyer (2013) identified six different interaction mechanisms between the cylinders, which were characterized by the angle of attack (α) and/or L/D . These mechanisms were boundary layer-cylinder interaction, shear layer or wake-cylinder interaction, shear layer-shear layer interaction, vortex-cylinder interaction, vortex-shear layer interaction, and vortex-vortex interaction. The vortex-cylinder interaction led to a significant fluctuating drag, while the vortex-shear layer interaction produced a high fluctuating lift.

For configurations comprising of three cylinders, Igarashi and Suzuki (1984) conducted an experimental study on the flow around three cylinders in tandem at Reynolds numbers ($Re = U_0 D/\nu$), with U_0 representing the free-stream velocity and ν denoting the kinematic viscosity of the fluid, ranging from 1.09×10^4 to 3.92×10^4 , and aspect ratios (L/D) varying from 1.0 to 4.0. Six flow patterns and two bistable flow regions were identified due to the dynamic effects of upstream-cylinder shear layers on the downstream cylinders. The flow around three-cylinder configurations, considering various gaps between the cylinders and both side-by-side and tandem arrangements, was numerically investigated by Harichandan and Roy (2010). The study revealed the presence of diverse wake patterns, including in-phase and anti-phase synchronized wake patterns, flip-flopping wake patterns, deflected wake patterns, and steady wake patterns. These wake patterns were found to be dependent on the Reynolds number and the gap spacing between the cylinders.

In hydro-environmental engineering applications, the proximity of a free surface in rivers of open-channel flows can significantly impact flow dynamics, potentially compromising the efficiency of in-stream leaky barriers. Sheridan et al. (1995, 1997) conducted one of the first experimental studies on a single horizontal cylinder positioned near a free surface, considering a range of Reynolds numbers ($5990 \leq Re \leq 9120$) and various submergence ratios (h/D , where h represents the distance between the upper surface of the cylinder and the undisturbed position of the free surface) within the range of $0 \leq h/D \leq 0.75$. They found that the unsteady development and interaction of three separated vorticity layers originating from the free surface, top, and bottom surfaces of the cylinder resulted in the formation of a jet-like flow with three distinct states, including a jet adjacent to the free surface, a jet adjacent to the base of the cylinder, and a metastable state.

Carberry (2002) conducted a series of experiments at a moderate $Re = 2,100$ to investigate the wake states as the cylinder approaches the free surface. They identified three distinct wake states that occurred as h/D decreased, that is, modified Kármán wake when $0.5 < h/D < 3.0$, flow attachment to the free surface when $0.125 < h/D < 0.5$, and a separated jet when $h/D < 0.125$. Bouscasse et al. (2017) adopted a Smoothed Particle Hydrodynamics (SPH) method to simulate the flow fields around partially and fully submerged circular cylinders at $Re = 180$. They found that wake behavior is dependent on the Froude number and the submergence ratio, and the cylinder experiences a downward lift when h/D is less than 0.5. While other numerical studies exist on the free surface effect on the flow hydrodynamics, these simulations are limited to single-cylinder configurations (Alzabari et al., 2023) and two-dimensional scenarios at low Reynolds numbers in the laminar flow regime (Chu et al., 2018; Moballa et al., 2020; Reichl et al., 2003, 2005), among others.

The flow around the three-cylinder design, of interest to stakeholders for leaky barriers in flood risk management, has limited applicability due to the lack of consideration of the free surface effects, compared to a single cylinder or a pair of cylinders. This study aims to address this knowledge gap by using Large-eddy simulations (LES) to investigate the flow past a leaky barrier composed of three circular cylinders. The configurations examined include one main configuration with three circular cylinders aligned vertically (Figure 1b) (zero angle, γ) and six additional configurations where the cylinders are inclined at angles of $\gamma = 15^\circ, 30^\circ$, and 45° to the upstream and downstream directions. The ultimate objective of this research is to enhance the application of in-stream leaky barriers by providing information on log inclination and barrier-induced sediment transport to inform natural flood management and river restoration schemes. This paper is structured as follows. Section 2 introduces the in-house Hydro3D code, numerical schemes, and computational setup. Section 3 introduces and discusses the flow hydrodynamics and structural response associated with the different LB designs. Finally, Section 5 presents the conclusions of this study and provides several recommendations for further research.

2. Numerical Framework

2.1. Computational Model

The open-source code Hydro3D is adopted to perform Large-Eddy Simulation (LES), which uses the spatially filtered Navier-Stokes equations for turbulent, incompressible, three-dimensional flow (Ouro et al., 2019, 2021). The code has been validated and applied in many engineering cases and in free-surface turbulent flows such as flow over bridge abutments (Kara et al., 2015), free-surface flow over square bars (Jalalabadi et al., 2021; McSherry et al., 2018) or rough beds (Bomminayuni & Stoesser, 2011; Liu et al., 2017; Nikora et al., 2019), tidal steam turbines (Ouro et al., 2024; Ouro & Nishino, 2021), solitary waves (Christou, Xie, et al., 2021), wave-

structure interaction (Christou, Stoesser, & Xie, 2021), submerged cylinder (Alzabari et al., 2023), and backward-facing step (Luo et al., 2023).

Hydro 3D is a finite-difference solver that uses a staggered Cartesian grid, where velocity components are specified at the center of cell faces and pressure is stored at the cell centers (Ouro et al., 2021). The governing equations employed to solve the filtered Navier-Stokes equations for two-phase, incompressible flows are as follows:

$$\frac{\partial u_i}{\partial x_i} = 0 \quad (1)$$

$$\frac{\partial u_i}{\partial t} + \frac{\partial u_i u_j}{\partial x_j} = -\frac{1}{\rho} \frac{\partial p}{\partial x_i} + \nu \frac{\partial^2 u_i}{\partial x_j \partial x_j} - \frac{\partial \tau_{ij}}{\partial x_j} + f_i + F_{sf} + g_i \quad (2)$$

where u_i and u_j are the resolved velocity components (i or $j = 1, 2$, and 3 represent the x , y , and z directions, respectively). Similarly, x_i and x_j represent the spatial directions. ρ is the density of the fluid, p is the resolved pressure, ν is the fluid kinematic viscosity, and τ_{ij} is the subgrid-scale (SGS) stress tensor. The forcing term f_i corresponds to the immersed boundary (IB) method that defines the solid geometries using the direct forcing technique described by Uhlmann (2005), which imposes a no-slip condition at the immersed-boundary points comprising the geometry of the cylinders. F_{sf} is the surface-tension force, and g_i is the gravitational acceleration.

Different scales of motion are characteristic of turbulent flows, and in the LES approach, large-scale motions are directly solved while small-scale motions are approximated via a sub-grid scale model (Stoesser, 2014). The wall-adapting local eddy-viscosity (WALE) sub-grid scale model (Nicoud & Ducros, 1999) is used to represent motion scales smaller than the grid size. Although the code includes other sub-grid scale models such as Smagorinsky, WALE is chosen for its compatibility with the immersed boundary method (Adzic et al., 2022).

Time advancement of the governing equations is achieved through the fractional step method, which is coupled with an explicit, low-storage, third order Runge-Kutta scheme. A second-order central differencing scheme approximates diffusive terms, while the fifth order weighted, essentially non-oscillatory (WENO) scheme calculates the convective velocity fluxes in the momentum conservation equation. The main advantage of using the WENO scheme is that it offers a reasonable compromise between the numerical stability and physical accuracy of modeling free surface flows (Ouro et al., 2021). The code runs in parallel on a high-performance computer by employing domain decomposition and message passing interface (MPI) protocols for communication between sub-domains.

Hydro3D adopts the Level-Set Method (LSM) that was developed by Osher and Sethian (1988), to resolve Eulerian-Eulerian multi-phase flows defining a continuous level-set function, ϕ , to determine the fluid density and viscosity fields across the computational domain. The level set function assigns positive and negative values according to the fluid in each grid cell. In the present study, the LSM employs a level set signed distance function, ϕ , which has zero value at the phase interface and is negative in air and positive in water. Employing a Heaviside function $H(\phi)$, fluid properties such as density (ρ) and viscosity (μ) are defined in a way that ensures a smooth transition across a layer of thickness $\varepsilon = 2.0\Delta x$, as shown:

$$\rho(\phi) = \rho_a + (\rho_w - \rho_a)H(\phi), \quad \mu(\phi) = \mu_a + (\mu_w - \mu_a)H(\phi) \quad (3)$$

where w and a are subscripts for water and air, respectively. The smoothed Heaviside function is defined as:

$$H(\phi) = \begin{cases} 0 & \text{if } \phi < -\varepsilon \\ \frac{1}{2} + \frac{1}{2} \left[\frac{\phi}{\varepsilon} + \frac{1}{\pi} \sin \left(\frac{\pi\phi}{\varepsilon} \right) \right] & \text{if } |\phi| \leq \varepsilon \\ 1 & \text{if } \phi > \varepsilon \end{cases} \quad (4)$$

In contrast to the standard rigid-lid approach where the air-water interface is fixed as the upper boundary condition, free-surface flows resolved with LSM have an additional computational overhead (Ouro et al., 2021). LSM

requires the resolution of a non-linear hyperbolic advection equation, which is approximated with the fifth-order WENO in addition to the mass and momentum conservation equations, to accurately capture the transport of ϕ :

$$\frac{\partial \phi}{\partial t} + u_i \frac{\partial \phi}{\partial x_i} = 0 \quad (5)$$

The mass conservation criteria of $|\nabla \phi| = 1$ is not directly satisfied due to the intrinsic nature of the advection equation. Consequently, the LSM is re-initialized to ensure that this condition is satisfied at every time step that is necessary to maintain mass conservation between the two fluids (Sussman et al., 1994).

A continuous surface force (CSF) (Yokoi et al., 2016) has been integrated into Hydro3D to ensure the accuracy of free-surface simulations in cases where there is significant surface breaking and air trapping, which leads to the formation of tiny droplets and bubbles in the fluid. The surface-tension force F_{sf} is defined by the traditional method as:

$$F_{sf} = \sigma k \delta(\phi) n_i \quad (6)$$

However, an enhanced method for calculating surface tension has been incorporated, which relies on a density-scaled delta function (δ^{scaling}). This approach, as outlined in Bussmann et al. (2000) and Yokoi (2013), improves numerical stability by directing the delta function (δ) toward the fluid with higher density. Accordingly, the surface tension force F_{sf} using this enhanced method is:

$$F_{sf} = \sigma k \delta^{\text{scaling}}(\phi) n_i, \quad \delta^{\text{scaling}} = 2H(\phi)\delta(\phi) \quad (7)$$

In both methods, σ represents the surface-tension coefficient ($\sigma = 0.728$), k is the curvature of the interface, and n_i is the unit vector normal to the liquid interface. They are computed as:

$$k = -\nabla \cdot n_i, \quad n_i = \frac{\nabla \phi}{|\nabla \phi|} \quad (8)$$

The smoothed delta function, $\delta(\phi)$ used in Equation 6 is a representation of the spatial derivative of the Heaviside function, which is specified in Equation 4. The definition is given by:

$$\delta(\phi) = \begin{cases} \frac{1}{2} \left(1 + \cos \frac{\pi \phi}{\varepsilon} \right), & \text{if } |\phi| < \varepsilon, \\ 0, & \text{otherwise.} \end{cases} \quad (9)$$

2.2. Computational Setup

The present model setup builds on the design principles of the ‘‘Shropshire Slow the Flow-Seven Tributaries’’ project (Follett & Wilson, 2020), which implemented large-scale natural leaky barriers for flood mitigation. The experimental study by Müller et al. (2021a, 2021b) scaled down these full-scale natural leaky barrier characteristics for lab-scale testing. This scaling process, detailed in Follett and Wilson (2020) and Müller et al. (2021a, 2021b), ensured that key hydrodynamic characteristics such as flow resistance and porosity were preserved.

The experimental setup of Müller et al. (2021a, 2021b) who studied short porous leaky barriers in lab-scale open channel flow is adopted in this study and expanded upon to explore additional configurations. The main design, referred to as S0 in this study, replicates the experiment and consists of three rows of horizontal cylinders with a diameter (D) of 0.025 m (Figure 2). These cylinders span the entire width of the main channel and are arranged such that there is a vertical gap (b_o) of 0.05 m ($2D$) from the bottom wall to the lower side of the barrier. Moreover, there is a vertical distance (b) of $0.5D$ between the logs, allowing flow to pass through the barrier. The leaky barrier has a height (H_S) of 0.1 m ($4D$) and a longitudinal length (L_S) equal to the cylinder diameter (Figure 2b). The backwater rise (ΔH) is calculated as the difference between the upstream (H_1) and downstream (H_2) water depths. The bulk velocity (U_0) in the experiment was set to 0.29 m/s, resulting in a bulk Reynolds number

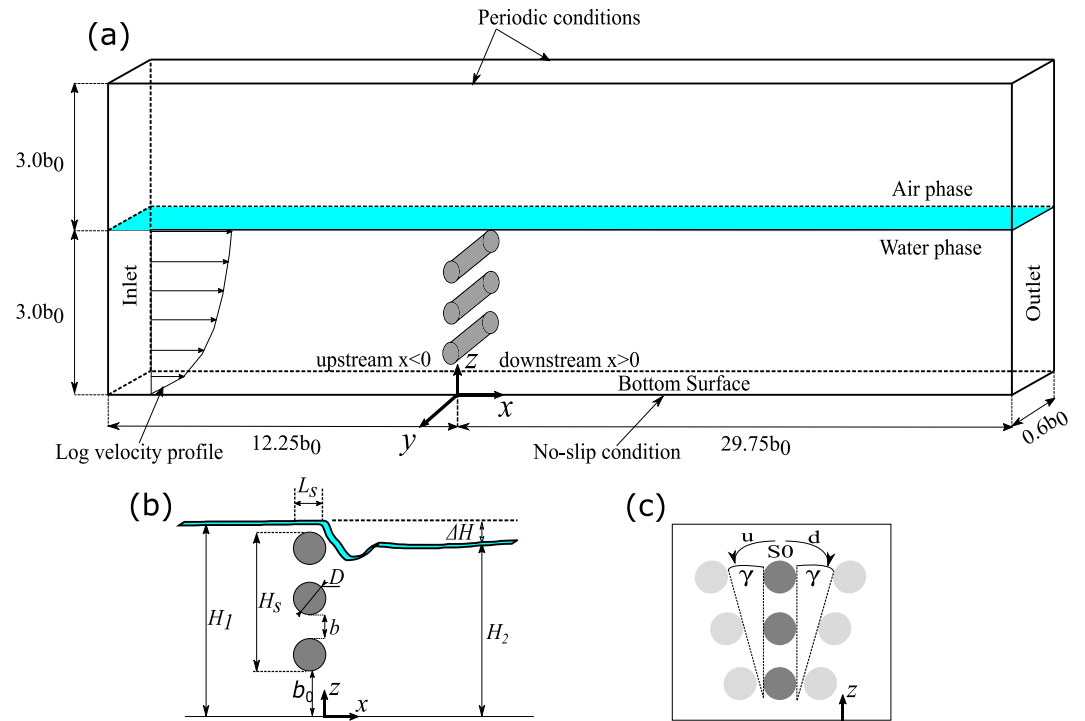


Figure 2. (a) Schematic of the computational domain adopted in the two-phase LES depicting the main characteristics of a leaky barrier structure. The inflow boundary conditions with a logarithmic approaching velocity profile are also indicated. (b) The structure has a height H_s and a longitudinal length L_s , with vertical inter-log gaps b and a vertical gap between the structure and the bottom wall b_0 . H_1 and H_2 represent the mean upstream and downstream flow depths, respectively. The structure is composed of horizontal channel spanning cylinders of diameter D aligned perpendicular to the flow direction. (c) The leaky barrier is inclined at different angles (γ), where d and u indicate the direction of the barrier inclination in the downstream and upstream directions, respectively.

($Re = U_0H/\nu$) of 43,500. The mean water depth (H) was 0.15 m, adopted as the initial condition according to the experiments, which gives a Froude number ($Fr = U_0/\sqrt{gH}$) of 0.24.

The computational domain, depicted in Figure 2a, has dimensions of 2.1, 0.3, and 0.03 m in the streamwise (x), vertical (z) and spanwise (y) directions, respectively. The top cylinder is positioned $12.25b_0$ downstream of the upstream inlet, and is the origin of the x -coordinates. Six additional configurations are numerically investigated by varying the inclination angles of the barrier, set at $\gamma = 15^\circ, 30^\circ$, and 45° , determined based on the vertical offset from the primary configuration (S0) (Figure 2c) and denoted as S1u, S2u and S3u, and S1d, S2d and S3d, where u and d represent upstream and downstream directions, respectively. For clarity, S1u and S1d are inclined at an angle of 15° , S2u and S2d at 30° , and S3u and S3d at 45° . Table 1 summarizes the main parameters used for all configurations.

A convective boundary condition is used at the outflow, and a no-slip boundary condition is applied to the bottom boundary. Periodic boundary conditions are used for the spanwise direction. The level-set method is employed to compute the water surface and the top of the domain is treated with a slip condition. The time step is variable, with a Courant-Friedrichs-Lewy condition of 0.2 to ensure numerical stability. The grid is uniform throughout the domain, with a resolution of $\Delta x/D = 0.03$, $\Delta y/D = 0.06$, and $\Delta z/D = 0.024$ in the x , y , and z directions, respectively. The numerical mesh consists of 28 million grid cells, or $N_x \times N_y \times N_z = 2800 \times 20 \times 500$, where N_{xi} denotes the number of grid nodes in each spatial direction. The simulations are executed on 350 CPUs, and each case is simulated for 35–40 flow-through periods ($T_f = L_x/U_0$, where L_x is the length of the domain) to compute mean flow statistics once the flow is fully developed. In the following, the symbols $\langle \cdot \rangle$ indicate time-averaging operation.

Table 1
Summary of Main Parameters for the Different Simulations

Configuration	Barrier angle (γ)	Direction	b (m)	b_0 (m)	U_0 (m/s)	Re	H (m)	Fr
S0	–	–	0.025	0.05	0.29	43,500	0.15	0.24
S1u	15°	Upstream						
S1d	15°	Downstream						
S2u	30°	Upstream						
S2d	30°	Downstream						
S3u	45°	Upstream						
S3d	45°	Downstream						

Note. b : Vertical distance between rows, b_0 : Bottom distance from wall, U_0 : Bulk velocity, Re: Reynolds number, H : Water depth, Fr : Froude number.

The current LES setup adopts a mean logarithmic velocity profile by setting a smooth log-law distribution at the domain inlet, using a friction velocity (u_*) of 0.0193 m/s, derived from the best-fit of the experimental velocity measurements (Müller et al., 2021a, 2021b):

$$\frac{u(z)}{u_*} = \frac{1}{\kappa} \ln \left(\frac{z u_*}{\nu} \right) \quad (10)$$

Here $\kappa = 0.41$ is the von-Kármán constant. To assess the appropriateness of using this mean logarithmic velocity profile at the inlet, Figure 3 presents vertical profiles of normalized mean streamwise velocity $\langle u \rangle / U_0$ at three stations upstream of the leaky barrier (S0), comparing LES with the experimental data. The LES results are generally consistent with the experimental results, quantified by the Root Mean Square Error (RMSE) and Mean Absolute Error (MAE), being 0.037 and 0.035 respectively, indicating a good agreement between LES and experimental data. At $x/b_0 = -4.0$, the $\langle u \rangle$ distribution is almost uniform along the water depth, while profiles closer to the upstream edge of the leaky barrier ($x/b_0 > -4.0$) show an increase of $\langle u \rangle$ along the bottom gap ($z/b_0 \leq 1$), while there is a reduction in $\langle u \rangle$ at higher water elevations ($z/b_0 > 1$) due to the vertical obstruction of the barrier and mass conservation, which causes the incoming flow to accelerate through the large gap beneath the structure.

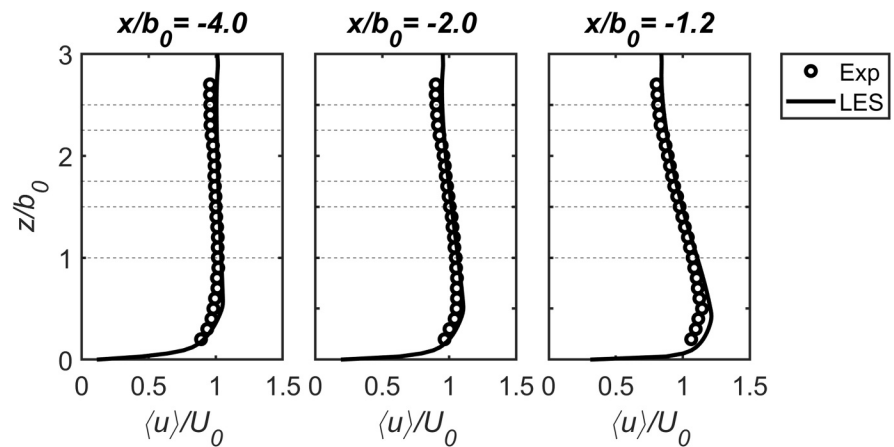


Figure 3. Vertical profiles of time-averaged streamwise velocity normalized by the bulk velocity $\langle u \rangle / U_0$ at three locations upstream of the leaky barrier. Comparison between experimental (symbols) and LES (lines) results. Horizontal dashed lines indicate log positions of the barrier.

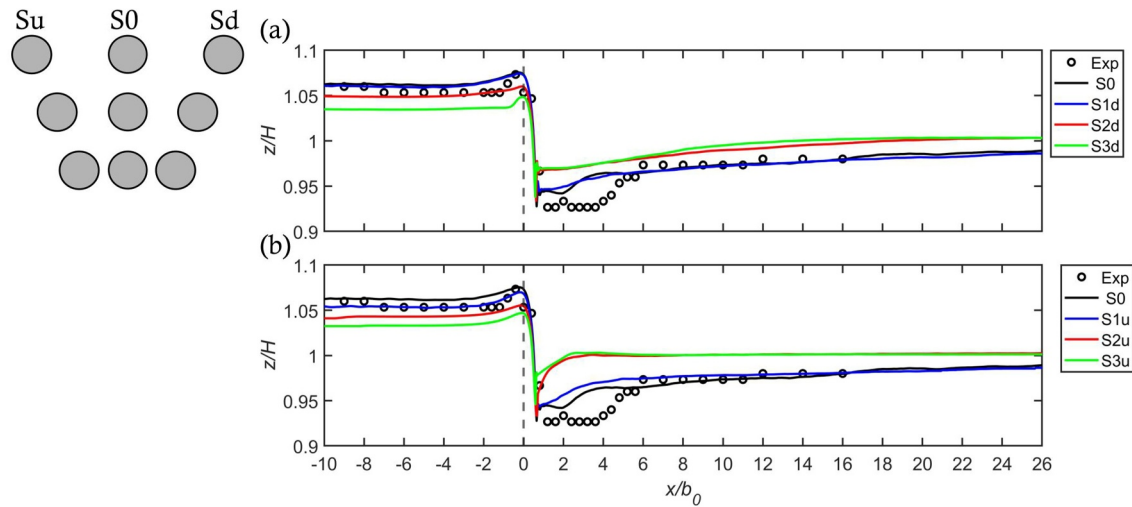


Figure 4. Free-surface profiles obtained from the LES for (a) downstream-inclined cases and (b) upstream-inclined cases along with experimental values of the non-inclined case (S0). Vertical dashed lines indicate the downstream edge of the top log, chosen as the origin of the x -coordinates.

3. Results and Discussion

This section will present the hydrodynamic characteristics of seven leaky barrier configurations. This includes examining the free-surface profiles, instantaneous flow field, time-averaged nature of the flow, recirculation regions, recovery of mean streamwise velocity, gap flow ratio, decay of the maximum jet velocity, potential bed scour, and hydrodynamic force coefficients.

3.1. Free Surface Profiles

The time-averaged water-surface profiles obtained from a previous experimental campaign for the vertical barrier (Müller et al., 2021a, 2021b), along with those derived from the current LES for various leaky barrier configurations, are presented in Figure 4. The development of the free-surface profile that results from the oncoming flow interacting with the porous obstructions is classified into three regions: (a) Backwater rise region ($x/b_0 < 0$), which is characterized by gradually varied flow conditions and an increase in the upstream water depth (H_1) relative to the undisturbed downstream water level (H_2); (b) Water-surface drop region ($x/b_0 \approx 0$), where a sudden decrease in water depth originates very close to the upstream edge of the barrier; and (c) Transition region, which extends between the water-surface drop until undisturbed downstream regions.

The end of the transition region corresponds to the downstream location where the slope of the mean water depth is nearly flat (Figure 4). For instance, in the S0 case and cases with the smallest angle (S1u and S1d), the downstream recovery region begins after a transition region of approximately $12b_0$, while this is at about $6b_0$ in the S2u and S3u cases. Conversely, for the S2d and S3d cases, the transition region extent is approximately at $18b_0$ (Figure 4).

Although the free-surface data that were obtained from the measurements and the LES for the non-inclined barrier (S0) exhibits a good agreement, the LES seems to slightly overestimate the experimental data at the positions of the drop in the free surface and in the transition region downstream of the barrier ($0 \leq x/b_0 \leq 5$). The results show that increasing the barrier's inclination to either upstream or downstream directions leads to a decrease in the backwater rise, which can reduce the incidence of overbank flow (Burgess-Gamble et al., 2017; Muhawenimana et al., 2023; Nisbet et al., 2015). Furthermore, the magnitude of the free surface drop varies with the angle of the barrier, that is, a flatter inclination corresponds to a smaller drop. Figure 4b shows that in comparison to the S0 layout, S1u exhibits a lower backwater rise and a higher water depth in the region immediately downstream ($x/b_0 \leq 10$), while the difference between S0 and S1d is negligible (Figure 4a). These differences between S1u and S1d cases compared to the S0 layout are associated with the direction of the flow going through the barrier's inter-log gaps, for example, in the upstream-inclined cases the flow is moves upwards toward the free surface.

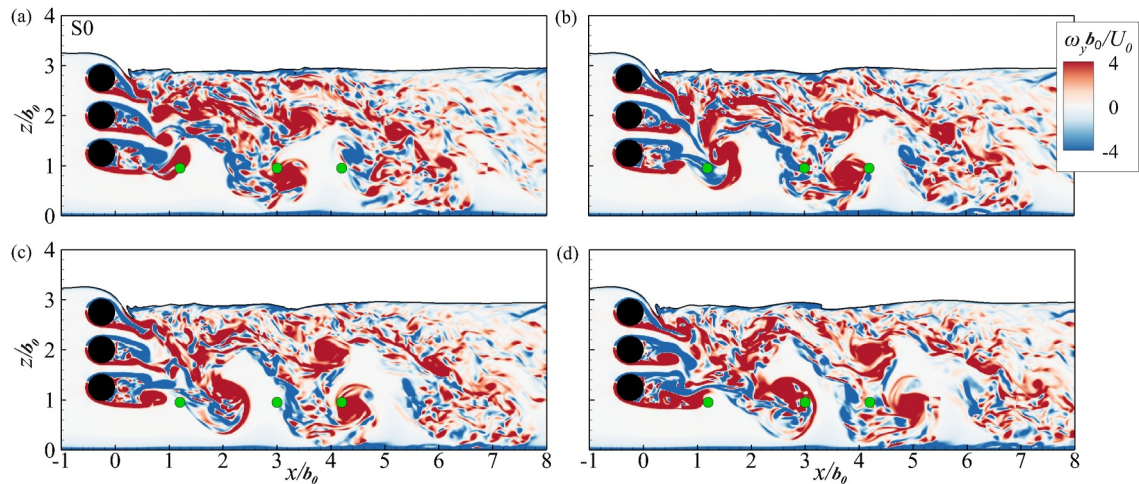


Figure 5. Contours of normalized vorticity over a vertical plane at the middle of the spanwise domain length for the non-inclined structure (S0), at four instants normalized by the peak frequency $t^* =$ (a) 3.9, (b) 4.2, (c) 4.5, and (d) 4.8. The free surface is depicted as a solid black line. The green circles denote the locations where velocity time series were extracted for the power spectral energy analysis.

3.2. Instantaneous Flow Field

The turbulent flow fields and vortex shedding developed behind the leaky barriers for all of the simulated configurations are analysed with contours of normalized spanwise vorticity over the xz -plane, along with pre-multiplied power spectral density computed from the vertical velocity fluctuations at various points downstream of the barriers. In the following, the vortex-shedding frequency (f_p) refers to the characteristic frequency at which vortices are periodically shed from the leaky barrier logs.

The instantaneous flow structures developed in the S0 design during four time instants covering the normalized time (t^*) range of $t^* = tf_p \in [3.9, 4.8]$, with t denoting time, are presented in Figure 5. The proximity of the submerged leaky barrier to the water surface creates a free-surface drop that constrains the wake behind the top log and affects the separation of the shear layers (Figure 5a for $t^* = 3.9$). This causes the upper shear layer to deflect downwards and merge with the lower shear layer, which inhibits the formation of roll-up shear layer vortices, as seen at $t^* = 4.2$ (Figure 5b). Meanwhile, the shear layers formed downstream of the lowermost logs are less influenced by the proximity to the free surface. At $t^* = 4.5$, the shear layers roll up, transitioning into von-Kármán vortices formed in the near wake, which then merge with the deflected shear layers from the top log in the region $1 \leq x/b_0 \leq 2$ (Figure 5c). These vortices interact with each other and merge the wakes into a wider one, a phenomenon known as vortex–vortex interaction regime (Alam & Meyer, 2013). Eventually, this results in the vertical location of the merged vortices being shifted toward the bottom wall at approximately $x/b_0 \approx 3$, as seen at $t^* = 4.8$ (Figure 5d). The von-Kármán vortices exhibit greater spatial coherence near the bottom wall compared to the upper water-column region near the free surface. Beyond $x/b_0 > 3$, coherent turbulent structures become larger spanning most of the water column.

The proximity interference, for example, when the cylinders are located close to each other, has an effect on vortex-shedding behavior. This interference can impact aspects such as the frequency of vortex shedding or the phase synchronization between the von-Kármán vortex street (Meneghini et al., 2001). Figure 6 shows the pre-multiplied power spectral density (PSD) in semi-log scale of the vertical velocity fluctuations from three sampling points (Figure 5), where the x -axis represents frequency (f) and the y -axis shows pre-multiplied PSD ($\phi \cdot f$). At $x/b_0 = 1.2$, an energetic peak is observed at a frequency of 4.53 Hz, indicating a coherent vortex shedding close to the barrier. The equivalent Strouhal number ($St = fD/U_0$) is 0.391, which is unchanged for the other streamwise locations at $x/b_0 = 3.0$ and 4.2. The amplitude of the pre-multiplied spectral energy decreases with increasing distance to the leaky barrier, indicating coherent vortex structures lose coherence.

In the downstream-inclined cases, further complexity is observed in the flow dynamics downstream of the barriers due to the combined effect of both the log's wakes and proximity interference (Figures 7a, 7c, and 7e). The separated free shear layers generated by the top log interact with the von-Kármán vortex formation of the lower

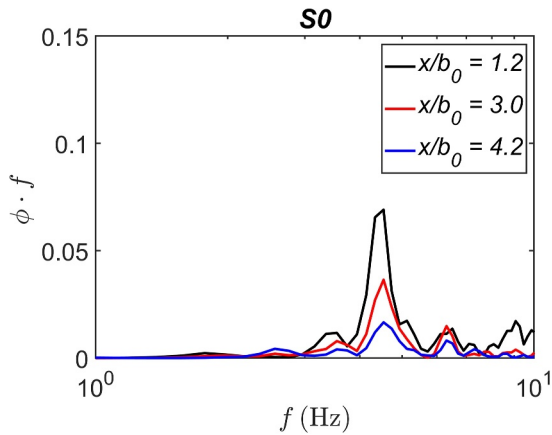


Figure 6. Pre-multiplied power spectral density (PSD) of the vertical velocity fluctuation (w') obtained at three points downstream of the barrier along the lower shear layer of the bottom log ($z/b_0 \approx 1.0$).

logs, as shown in Figure 7a for the S1d case ($x/b_0 \approx 1$). As the barrier angle increases, the occurrence of this interference is delayed to positions further downstream. This delay allows the shear layers of the lowermost logs to freely roll up and generate vortices in the near wake, before they interfere with each other when $x/b_0 > 1$. For the S3d configuration, the von-Kármán vortices detach and get advected toward to the bottom wall in comparison to the other cases, which results in a faster loss of coherence of the vortices as they travel further downstream (Figure 7e).

The pre-multiplied power spectral density (PSD) analysis reveals distinct vortex-shedding frequencies for each configuration. In the S1d case (Figure 7b), at $x/b_0 = 0.8$, the largest pre-multiplied spectral energy is seen at two frequencies of 5.26 Hz ($St = 0.453$) and 5.87 Hz ($St = 0.506$), while for downstream positions of $x/b_0 = 2.6$ and 3.8 the former has more energy. This suggests that the combination of vortex-shedding from the bottom-log and eventual combination with vortical structures from the mid-log at slightly lower frequencies. In the S2d layout (Figure 7d), the dominant frequency is 6.86 Hz ($St = 0.591$) for both $x/b_0 = 0.3$ and 2.1, reducing to 5.21 Hz ($St = 0.449$) at $x/b_0 = 3.3$. The amplitude is highest at $x/b_0 = 0.3$, and rapidly decreases at downstream positions, especially at $x/b_0 = 3.3$ where the initial vortex shedding from the individual logs transitioned into

larger vortical structures resulting from the merging of the logs' vortices (Figure 7c). In the S3d case (Figure 7f), the dominant frequency is 5.85 Hz ($St = 0.504$) across all evaluated positions ($x/b_0 = -0.3, 1.5, \text{ and } 2.7$). The

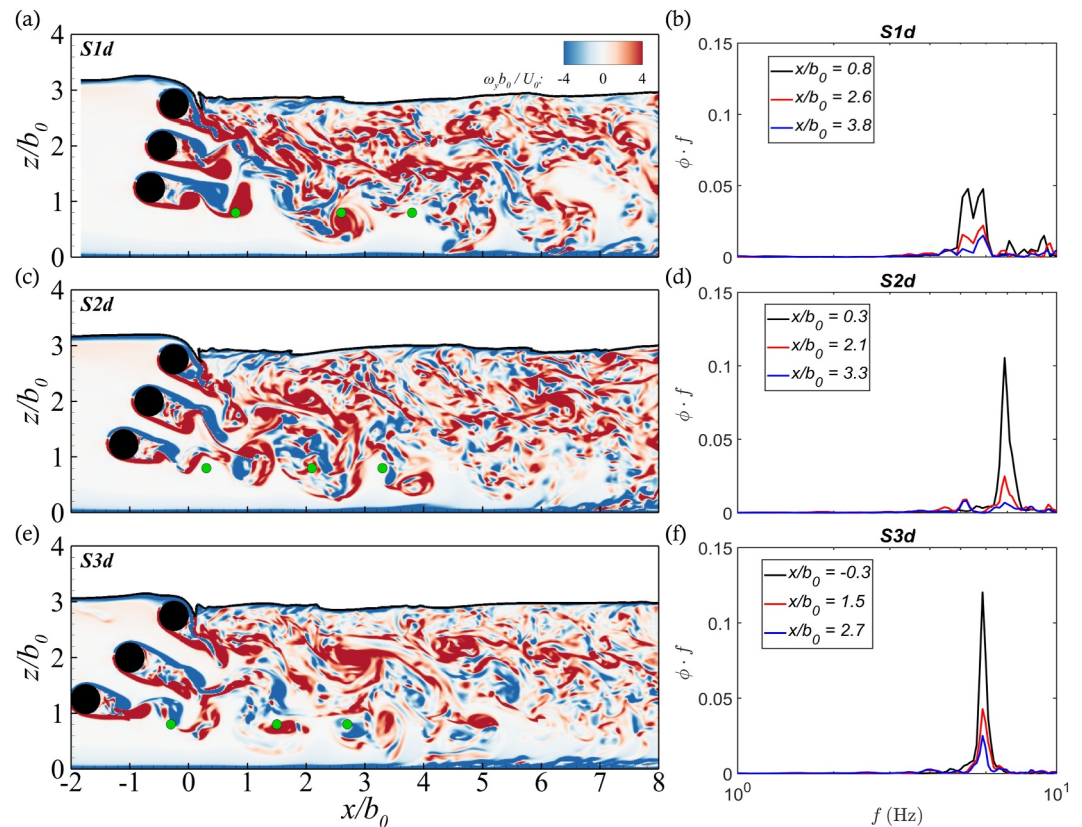


Figure 7. Contour plots of (a, c, e) normalized vorticity over a vertical plane at the middle of the spanwise domain length comparing the downstream-inclined structures (S1d, S2d, S3d), where the free surface is depicted as a solid black line. (b, d, f) Pre-multiplied power spectral density (PSD) of the vertical velocity fluctuation (w') computed at three points downstream of the barrier along the lower shear layer of the bottom log ($z/b_0 \approx 1.0$).

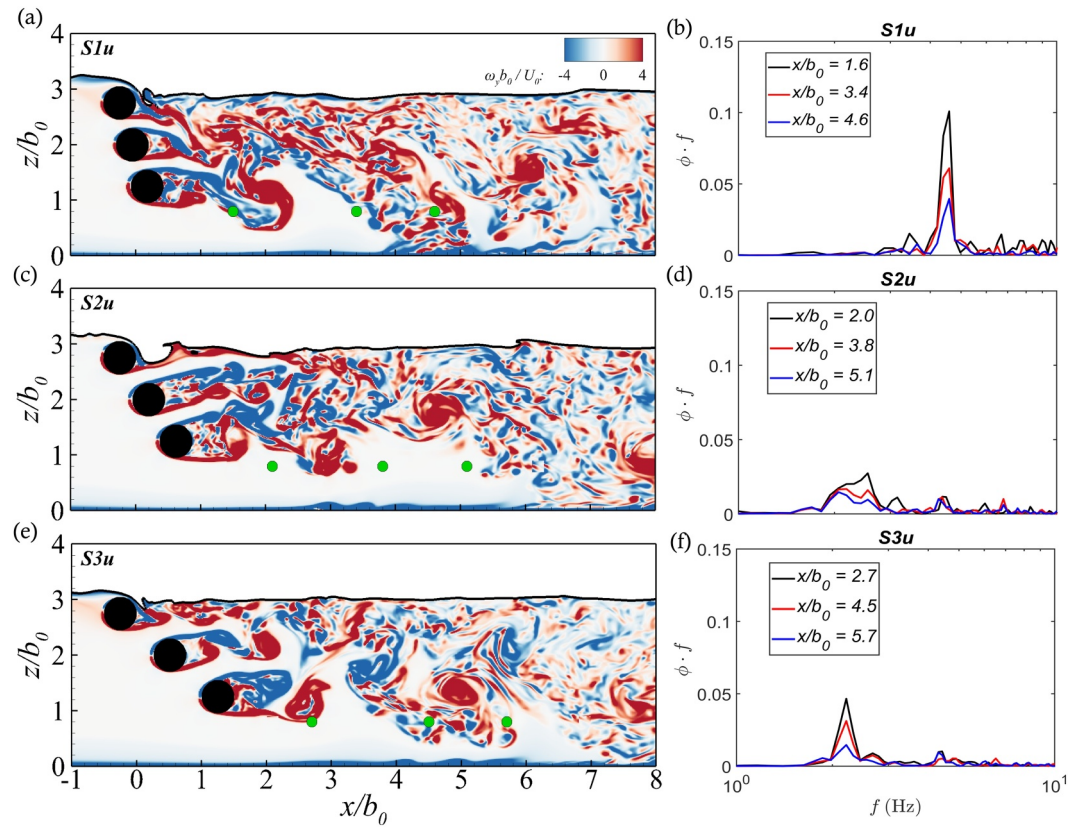


Figure 8. Contour plots of (a, c, e) normalized vorticity over a vertical plane at the middle of the spanwise domain length comparing the upstream-inclined structures (S1u, S2u, S3u). The free surface is depicted as a solid black line. (b, d, f) Pre-multiplied power spectral density (PSD) of the vertical velocity fluctuation (w') at three points downstream of the barrier along the lower shear layer of the bottom log ($z/b_0 \approx 1.0$).

spectral energy amplitude decreases downstream, with the highest amplitude at $x/b_0 = -0.3$ while relatively similar values are seen at $x/b_0 = 1.5$ and 2.7 . Unlike the other configurations, such as S2d, there is no transition in the shedding frequency at lower values, indicating that the vortex shedding coming from the individual logs remains coherent over longer distances downstream of the leaky barrier.

In the S1u setup, with an upstream inclination, the merged vortices in the near wake of the barrier continue to feature a downward movement (Figure 8a). The small-scale vortices tend to converge since their shedding until $z/b_0 = 2$ in the downstream region, and be convected downwards with the flow and eventually reaching the bottom wall at $x/b_0 = 4 - 5$. In the S2u case, there is a notable deformation of the free surface occurring behind the top log hinders the development of its shear layers, their combination and interaction with others (Figure 8c). This causes the vortices that are shed from the middle and bottom logs to travel upwards toward the free surface shortly after being shed, which triggers oscillations in water surface layer downstream of the barrier. This effect was not observed in downstream log configurations. When the barrier is largely inclined to the upstream direction, the wake interference becomes less apparent. The S3u design leads to negligible interactions between the vortices shed by the individual logs in the near wake region ($x/b_0 \leq 3$, Figure 8e). Compared to the upper water column region where the developed vortices decay faster as they impinge onto the free surface, the vortices at lower depths exhibit larger spatial coherence while they are convected downstream with the flow. For convenience, Supporting Information S2 are provided showing the instantaneous vorticity field around the cylinders in the inclined cases.

In the S1u layout (Figure 8b), the pre-multiplied spectra show dominant frequencies remain constant with downstream locations with value of 4.58 Hz ($St = 0.395$). In the S2u case (Figure 8d), the dominant frequency is 2.54 Hz ($St = 0.219$) at $x/b_0 = 2.0$, which is a significant reduction in the main shedding frequency compared to S1u but also there is a notable decay in the pre-multiplied spectral energy. At downstream stations of $x/b_0 = 3.8$

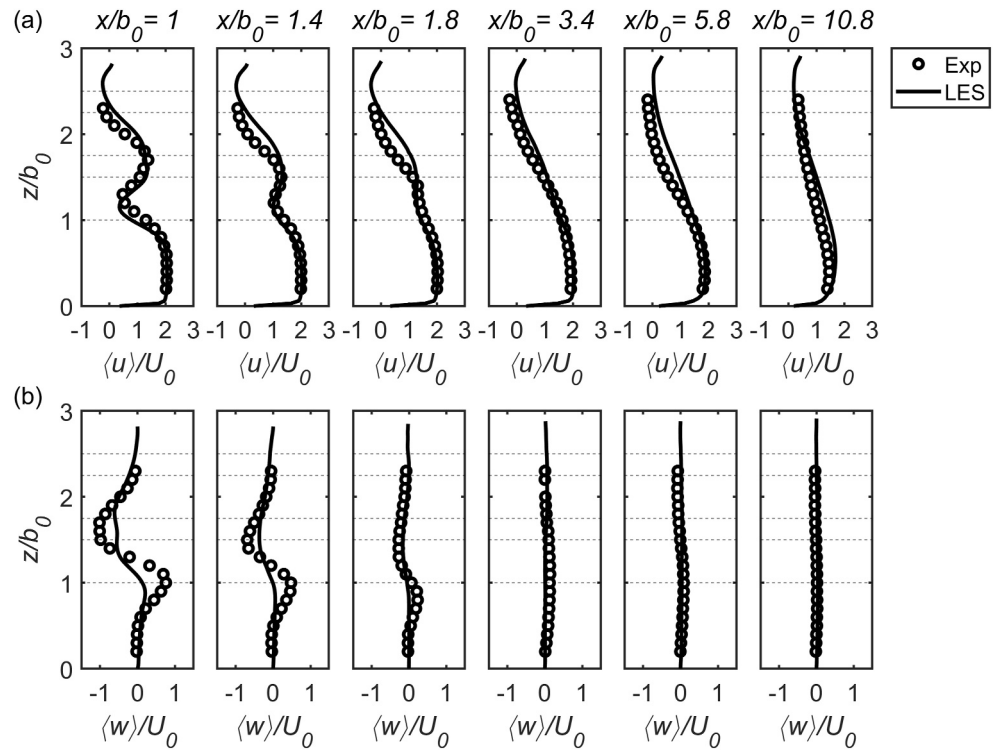


Figure 9. Vertical profiles of (a) normalized mean streamwise velocity $\langle u \rangle / U_0$ and (b) vertical velocity $\langle w \rangle / U_0$ at six locations downstream of the barrier. Comparison between experimental (symbols) and LES (lines) results. Horizontal dashed lines indicate the positions of logs.

and 5.1, the peak frequency shifts to about 2 Hz ($St = 0.172$). The S3u design (Figure 8f), vortex-shedding frequency is at 2.21 Hz ($St = 0.191$) across all positions. Similar to S2u, there is a noticeable reduction in amplitude compared to S1u, which is attributed to the setup of the configuration. For S2u and S3u, the von-Kármán are advected toward the upper water column region when moving downstream, with reduced interaction between vortices from the bottom log and the two upper ones.

3.3. Time-Averaged Flow Characteristics

Vertical profiles of normalized mean streamwise ($\langle u \rangle / U_0$) and vertical ($\langle w \rangle / U_0$) velocities at six locations downstream of the S0 case obtained from the LES and compared with the experiments (Müller et al., 2021a, 2021b) shown in Figure 9. In the near wake ($x/b_0 \leq 1.4$), the profiles feature a high-momentum region expanding from the bottom bed until the barrier's lower log location (Figure 9a). At $x/b_0 = 1$, the streamwise velocity decreases along the bottom log height ($1 < z/b_0 < 1.5$) as it corresponds to the log's wake, and increases along the lower inter-log gap ($1.5 < z/b_0 < 1.75$) which is the signature of the secondary jet whose velocity is smaller in comparison to that of the wall jet. Above $z/b_0 > 1.75$, the streamwise velocity experiences reduces again due to the wake of the second log and it then follows a slight increase at greater water heights ($z/b_0 \approx 2.75$), as a signature of the overtopping flow. As the downstream distance increases, the disturbance caused by the barrier's wake gradually reduces without the signature of the log's wakes after $x/b_0 = 3.4$. The distribution of the streamwise velocity agrees well between the experimental and the LES results, especially along the bottom gap ($z/b_0 < 1$).

The distribution of vertical velocity at the selected downstream stations (Figure 9b) reveals a predominant upwards fluid motion along the lower side of the lowest log ($z/b_0 = 1$) up to $x/b_0 \leq 1.8$, whereas a downwards motion is apparent along the lower inter-log gap ($1.5 < z/b_0 < 1.75$). At $x/b_0 \leq 1.4$, the peak $\langle w \rangle / U_0$ values are underestimated by the LES, but further downstream these differences gradually diminish.

Distributions of time-averaged second-order statistics, namely streamwise ($\langle u' \rangle / U_0$) and vertical ($\langle w' \rangle / U_0$) turbulence intensities, and vertical Reynolds shear stress $-\langle u' w' \rangle / U_0^2$, at six positions downstream of the barrier

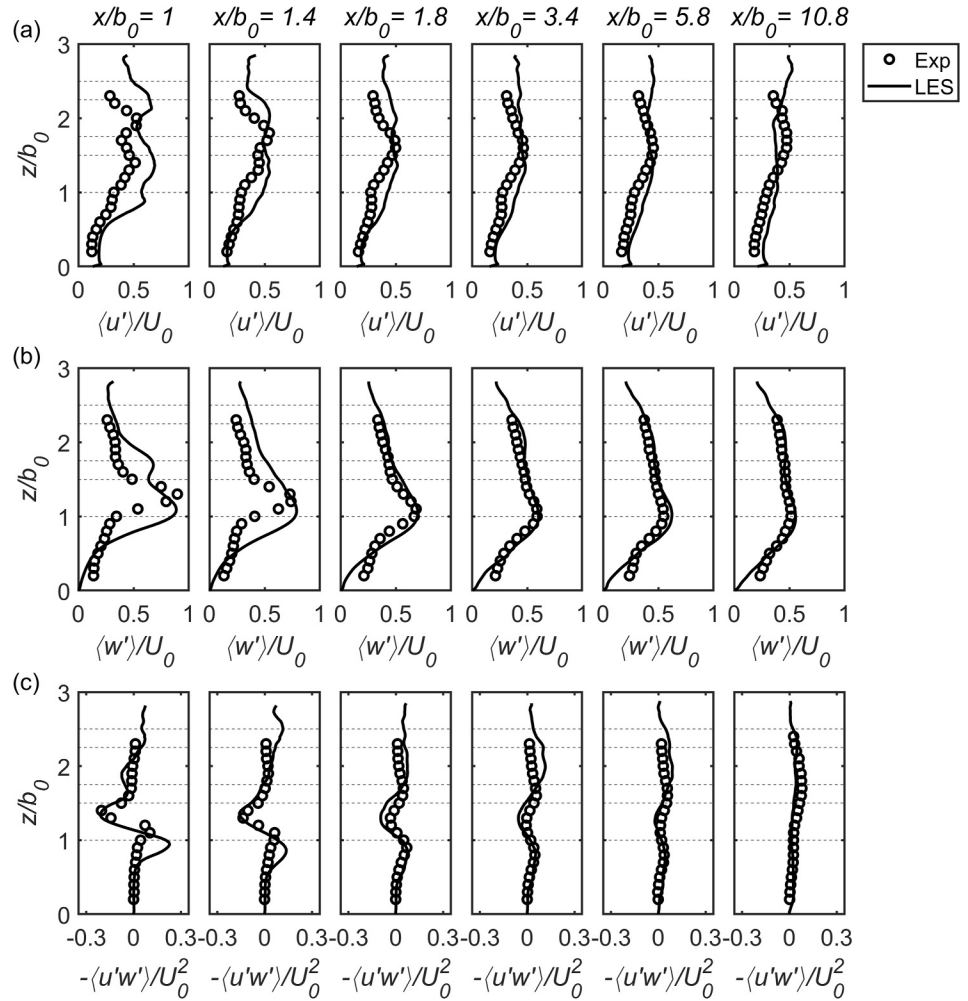


Figure 10. Vertical profiles of (a) streamwise turbulence intensity $\langle u' \rangle$, (b) vertical turbulence intensity $\langle w' \rangle$, and (c) vertical Reynolds shear stress $-\langle u'w' \rangle$ at different locations downstream of the barrier. Comparison between experimental (symbols) and LES (lines) results. Horizontal dashed lines indicate log positions.

are shown in Figure 10. At positions closer to the barrier ($x/b_0 \leq 1.4$), LES resolves higher streamwise turbulence intensity values than the experiment between $1 < z/b_0 < 2.75$ (Figure 10a). Further downstream, the variation in the vertical distribution of streamwise turbulence intensity reduces, improving a better agreement between the LES and experimental data. The vertical turbulence intensity profiles near the structure ($x/b_0 \leq 1.4$) indicate that maxima of $\langle w' \rangle$ are attained along the height of the lowest log (Figure 10b), with a slight downwards shift in the peak position observed in the LES data compared to the experiments. At $x/b_0 \geq 1.8$, the peak of $\langle w' \rangle / U_0$ is seen at a height of $z/b_0 \approx 1.0$ in both experimental and LES results. The agreement between the simulations and experiments improve further downstream across the whole water column. At $x/b_0 \leq 1.4$, the vertical profiles of $-\langle u'w' \rangle / U_0^2$ exhibit peak positive values at $z/b_0 = 1$, indicating upwards turbulent momentum exchange, while negative peak values are noted along the upper shear layer of the lowest log at $z/b_0 \approx 1.5$, indicating downwards turbulent momentum exchange (Figure 10c). With the exception of the LES overprediction of the peak vertical Reynolds shear stresses in the near wake at $x/b_0 \leq 1.4$ and $z/b_0 \approx 1$, the experimental and LES data demonstrate good agreement over the leaky barrier wake.

The upstream flow is characterized with velocity profiles presented in Figures 11 and 12, respectively. Figure 11 shows that as proximity to the barrier increases, the flow is diverted toward the barrier's lower gap ($0 \leq z/b_0 \leq 1$), featuring high streamwise velocities. The maximum streamwise velocity along the bottom gap at the nearest

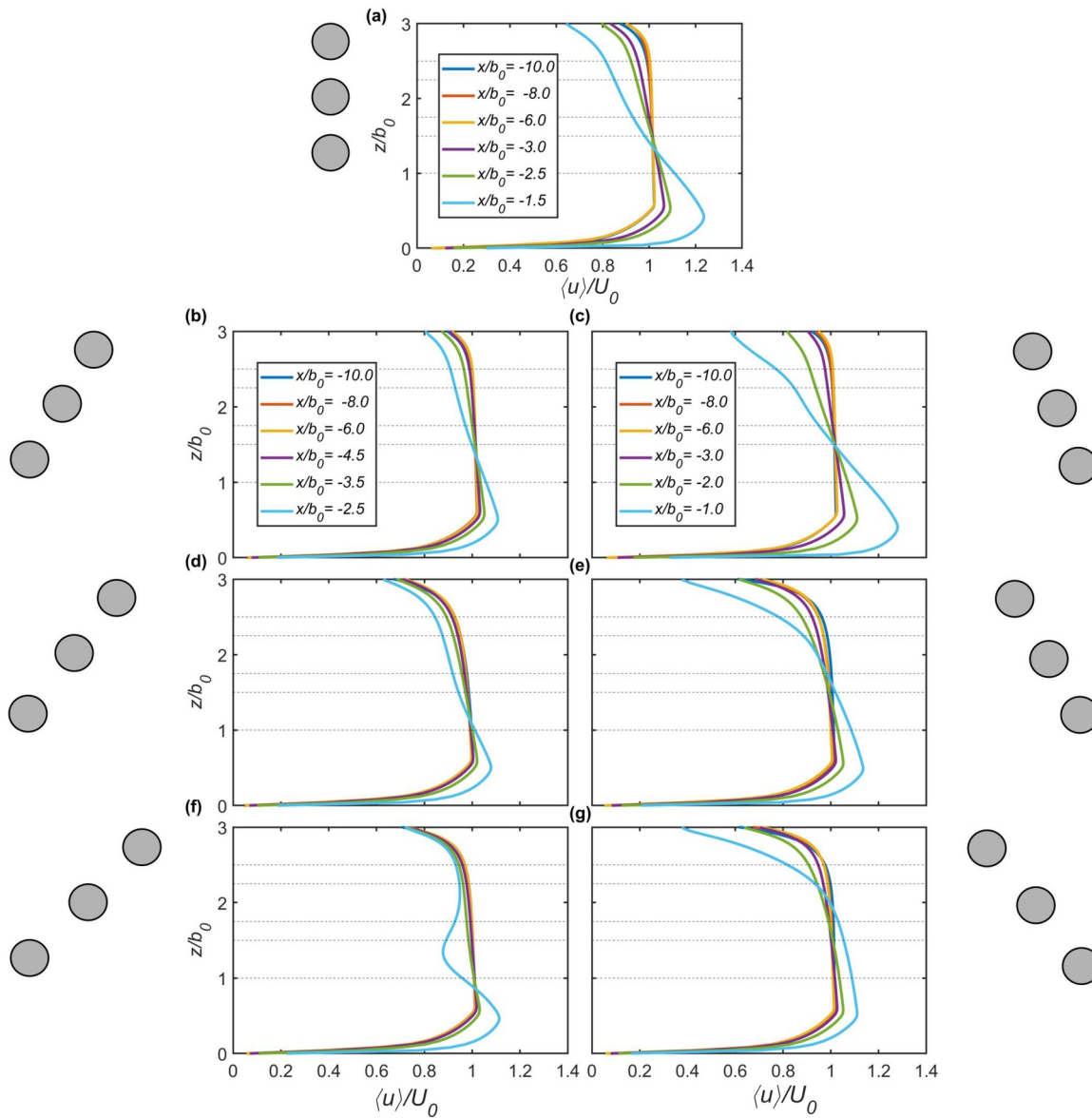


Figure 11. Vertical profiles of normalized mean streamwise velocities $\langle u \rangle / U_0$ at different locations upstream of the barrier for (a) the S0 case, (b, d, f) the downstream-inclined cases (S1d, S2d, S3d, respectively), and (c, e, g) the upstream-inclined cases (S1u, S2u, S3u, respectively). The dashed lines indicate the positions of the logs.

upstream profile exhibits slight variations among the leaky barrier design due to the relative position of the logs to the incoming flow. For instance, in the downstream-inclined cases at $x/b_0 = -2.5$, the largest velocity range between $\langle u \rangle / U_0 = 1.05 - 1.11$, while in the upstream-inclined layouts these range between $\langle u \rangle / U_0 = 1.11 - 1.28$ at $x/b_0 = -1.0$. For upstream-oriented designs, at the barrier's height ($z/b_0 > 1$), the streamwise velocities decrease with increasing vertical elevation, with a larger reduction as distance to the barrier reduces. Near the free surface, the S1u configuration exhibits a mean streamwise velocity of $\langle u \rangle / U_0 = 0.6$ at $x/b_0 = -1$ and $z/b_0 = 3.0$ (Figure 11c), in contrast to the lower value of $\langle u \rangle / U_0 = 0.4$ found in the more inclined S2u and S3u designs (Figures 11e and 11g). The downstream-inclined barriers also exhibit a decrease in the streamwise velocities but at a smaller rate. For instance, at $x/b_0 = -2.5$ and $z/b_0 = 3.0$, the velocity minimum for the S1d layout is $\langle u \rangle / U_0 = 0.8$ (Figure 11b), which reduces to about $\langle u \rangle / U_0 = 0.7$ for the S2d and S3d designs (Figures 11d and 11f).

In the distribution of the vertical velocity profiles ($\langle w \rangle / U_0$), the S0 design features a parabolic distribution for $x/b_0 < -3$, being the maximum velocity attained at $x/b_0 = -1.5$ along the center of the lowest log at

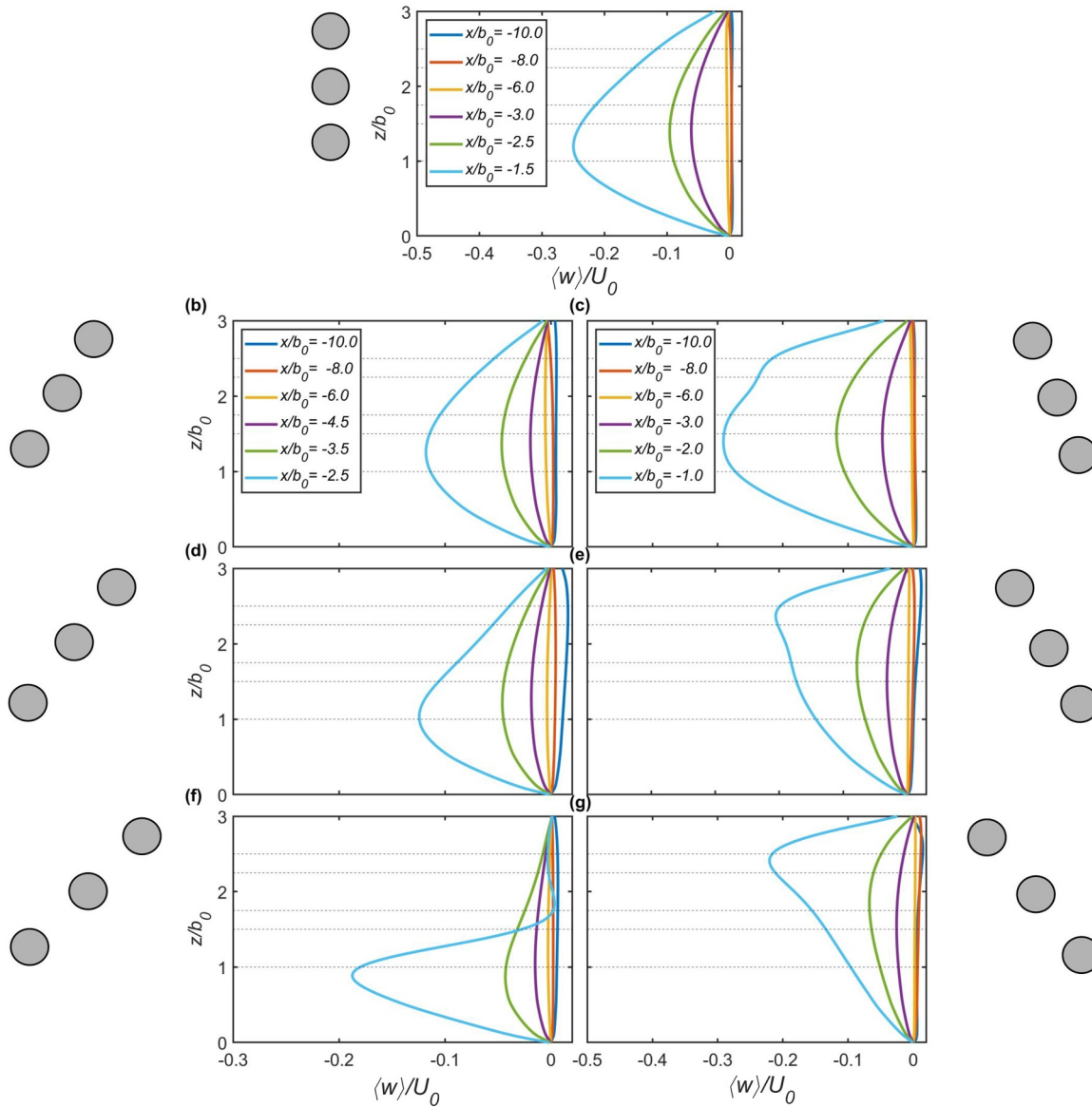


Figure 12. Vertical profiles of normalized mean vertical velocities $\langle w \rangle / U_0$ at different locations upstream of the barrier for (a) the S0 case, (b, d, f) the downstream-inclined cases (S1d, S2d, S3d, respectively), and (c, e, g) the upstream-inclined cases (S1u, S2u, S3u, respectively). The dashed lines indicate the positions of the logs.

$z/b_0 = 1.25$ and corresponds to a region of downward fluid motion (Figure 12a). At $(x/b_0 \geq -6)$, there are almost zero vertical velocity values as the effect from the barriers is negligible. In the S1d case, the vertical distribution of $\langle w \rangle / U_0$ resembles that of the S0 case, albeit with a reduced peak value of $\langle w \rangle / U_0 = -0.12$ (Figure 12b). The maximum vertical velocity in the S2d case is similar to that in S1d, although its position is slightly shifted to a lower vertical height at $z/b_0 = 1$. With a maximum velocity of $\langle w \rangle / U_0 = -0.19$ in the S3d layout, there is a noticeable shift of its position further downwards (Figure 12f).

For upstream-inclined designs, profiles of $\langle w \rangle$ exhibit a reversed pattern compared to the downstream-inclined barriers (Figures 12c, 12e, and 12g). At $x/b_0 = -1$, the upstream profiles for the S2u and S3u cases show an upwards shift in the position of the largest vertical velocities at $z/b_0 \approx 2.25 - 2.5$ with a peak value of $\langle w \rangle / U_0 \approx -0.2$. In contrast, the S1u layout reaches a peak magnitude of $\langle w \rangle / U_0 \approx -0.3$ at a similar vertical position as the S1d case together with larger velocities above the maximum. These differences between inclined barrier layouts in both directions is attributed to the alteration in the positioning of the logs in relation to the point of initial flow impingement.

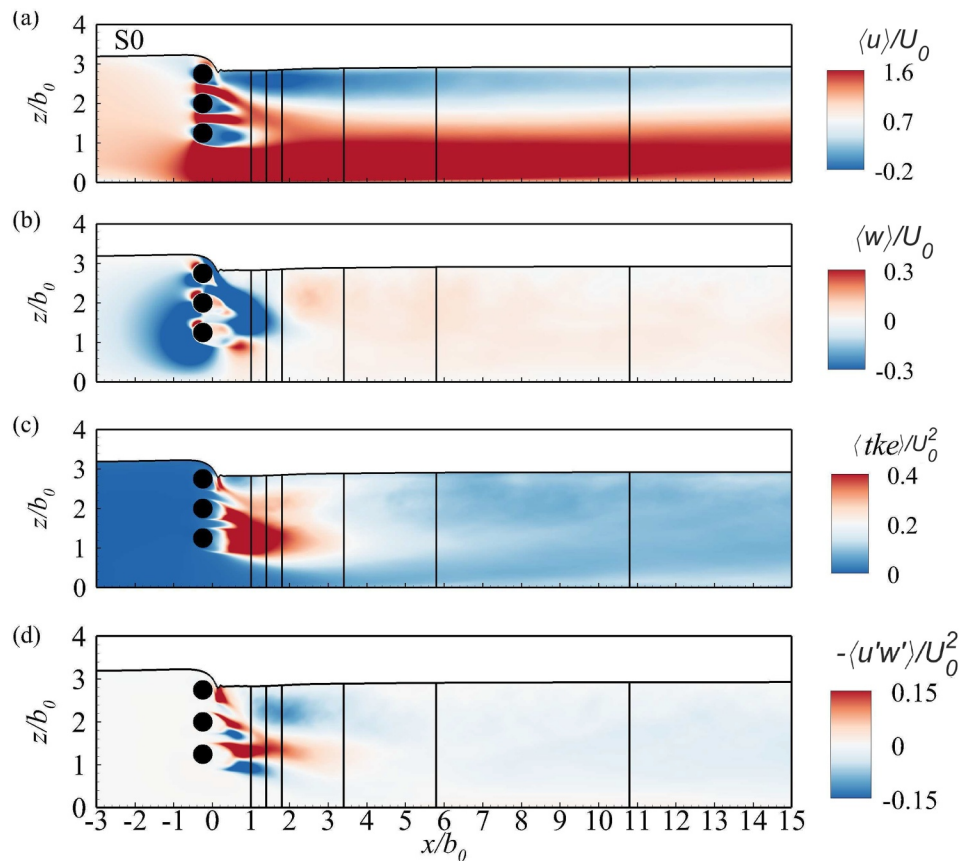


Figure 13. Side elevation contour plots of the LES computed (a) streamwise velocity, (b) vertical velocity, (c) turbulent kinetic energy, and (d) Reynolds shear stress, normalized by the bulk velocity for the S0 case. The vertical lines mark the locations at which vertical profiles of the mean quantities are plotted and shown in Figures 9 and 10.

The spatial distribution of the time-averaged flow field for the S0 design is shown in Figure 13 along the channel center-line plane, that is, at $y/b_0 = 0.3$. A high-momentum jet forms beneath the barrier, which is characterized by a significant increase in mean streamwise velocities (Figure 13a). This jet exhibits characteristics similar to a modified wall jet (Ead & Rajaratnam, 2002) or the flow beneath engineered or naturally formed logjam (Beebe, 2000) as it keeps its maximum velocity for a certain downstream distance before transitioning into a rapid decay, as explained later in Section 3.7. Behind the leaky barrier at $z/b_0 > 1$, the streamwise velocities gradually diminish, becoming significantly reduced closer to the free surface. The inter-log gaps of the barriers allow for distinct internal flow paths, generating secondary jets, known as offset jets, which influence near wake decay and turbulent mixing (Wang & Tan, 2007). Figure 13a shows how these parallel offset jets deflect downwards and eventually merge with the main wall jet at $x/b_0 \approx 2 - 3$.

Figure 13b presents the contours of time-averaged vertical velocities, revealing two distinct regions of high negative vertical velocities indicating the downwards motion of the flow. The first is situated upstream of the barrier along its lower part ($z/b_0 < 2$), which results from the vertical obstruction caused by the barrier. The second region is adjacent to the downstream side of the barrier, extending from the free surface downwards down to the upper shear layer of the lowest log, reflecting the downwards motion of flow overtopping the barrier and flow penetrating the structure through the inter-log gaps. A small region of positive vertical velocities is found downstream of the leaky barrier, in close proximity to the bottom log, which indicates the upwards vertical motion of the wall-jet flow.

Figure 13c presents the contours of the time-averaged turbulent kinetic energy (*tke*) distribution, revealing high *tke* levels over the wake region of the middle and bottom logs until $x/b_0 \approx 2$. This region indicates the high turbulence in the immediate recirculation zones behind the logs, which coincides with low streamwise velocities

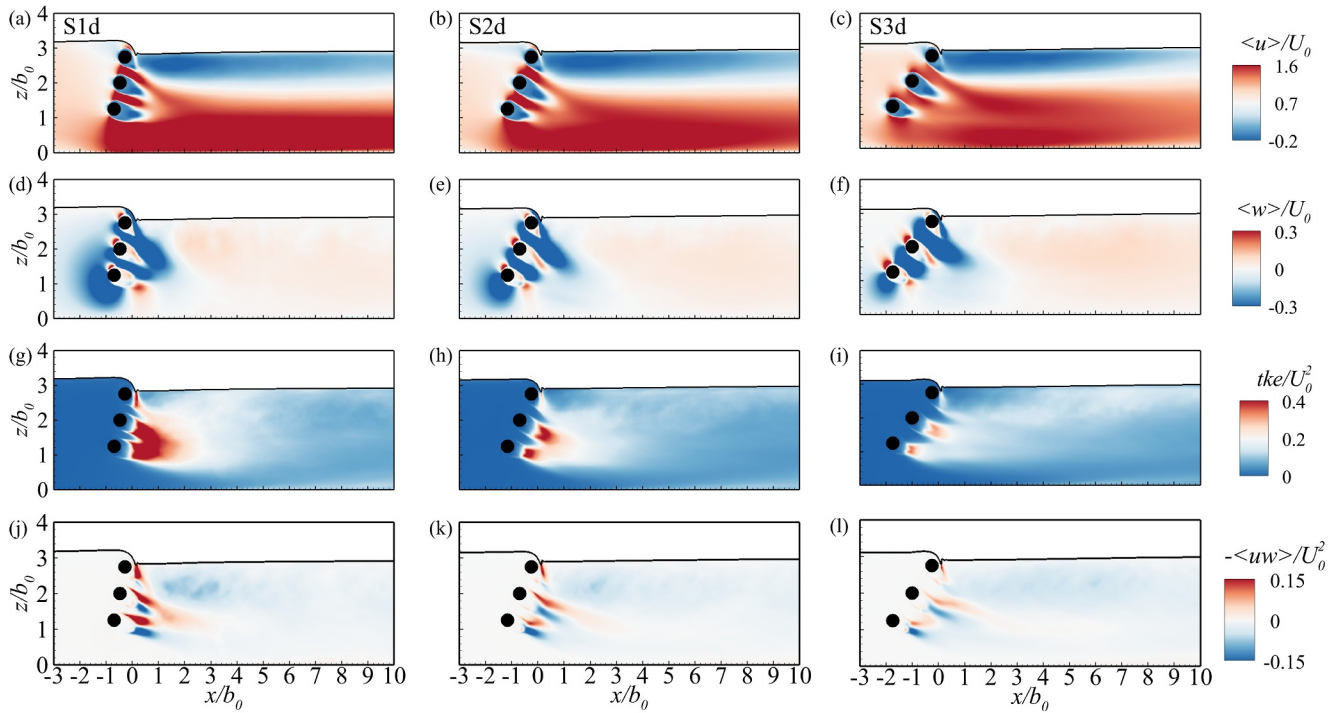


Figure 14. Side elevation contour plots of the LES computed (a–c) streamwise velocity, (d–f) vertical velocity, (g–i) turbulent kinetic energy, and (j–l) Reynolds shear stress, normalized by the bulk velocity for the downstream-inclined cases (S1d, S2d, and S3d).

(Figure 13a). The evolution of the shear layers shed from the logs and the interaction of the secondary jets downstream of the barrier are the main contributors to these high levels of the *tke* (Figure 13c). Figure 13d shows that vertical Reynolds shear stress have larger values along the upper side of the bottom log, indicating a greater momentum exchange between the flow over the bottom log and its near wake. Likewise, the middle log shows a similar pattern, albeit with lower levels of $-\langle u'w' \rangle / U_0^2$, as a result of a reduced momentum exchange compared to the bottom log. The top log exhibits a weak turbulent momentum exchange. Moreover, an additional area of high turbulent momentum exchange is found below the free surface at $1 \leq x/b_0 \leq 3$.

Figures 14a–14c show the streamwise velocity contours in the downstream-inclined cases. In the S1d case, no significant changes are observed compared to the S0 case, while in the S2d and S3d cases the magnitudes of the streamwise velocity remain relatively high downstream before exhibiting a notable reduction at far downstream positions ($x/b_0 \geq 10$). For instance, at $x/b_0 = 10$, the maximum streamwise velocity along the bottom gap decreases as the angle of barrier increases, with $\langle u \rangle / U_0 = 1.8, 1.5$ and 1.3 for S1d, S2d, and S3d, respectively. Furthermore, the increase in the angle of the barrier results in a decrease in the magnitude of streamwise velocities within the inter-log gaps, with average values of $\langle u \rangle / U_0 = 1.9, 1.7,$ and 1.5 for the S1d, S2d, and S3d barriers, respectively. The downstream-inclined cases also exhibit a decrease in $\langle u \rangle / U_0$ close to the free surface, mainly due to the diverted fluid motion toward the bottom wall downstream of the barrier.

The downstream-inclined cases do not exhibit significant changes in the regions of negative vertical velocity downstream of the barrier (Figures 14d–14f), with the offset jets through the inter-log gaps becoming either detached or merged depending on the inclination angle of the barrier. Furthermore, upstream of the barrier's lower side, the regions of the negative $\langle w \rangle / U_0$ reduce as the angle of barrier increases due to a lower flow diversion toward the bottom gap. Contours of mean turbulent kinetic energy (*tke*) reveal show that the S1d design exhibits almost similar distribution to the non-inclined case (S0). However, *tke* levels significantly reduce as the angle of barrier increases (S2d and S3d). Analogously, the magnitude of vertical Reynolds shear stresses decrease as the angle of barrier increases (Figures 14j–14l).

In the upstream-inclined layouts, the increase in the inclination angle results in a decrease in streamwise velocities (Figures 15a–15c), implying a shorter longitudinal extent of the region dominated by high streamwise velocities

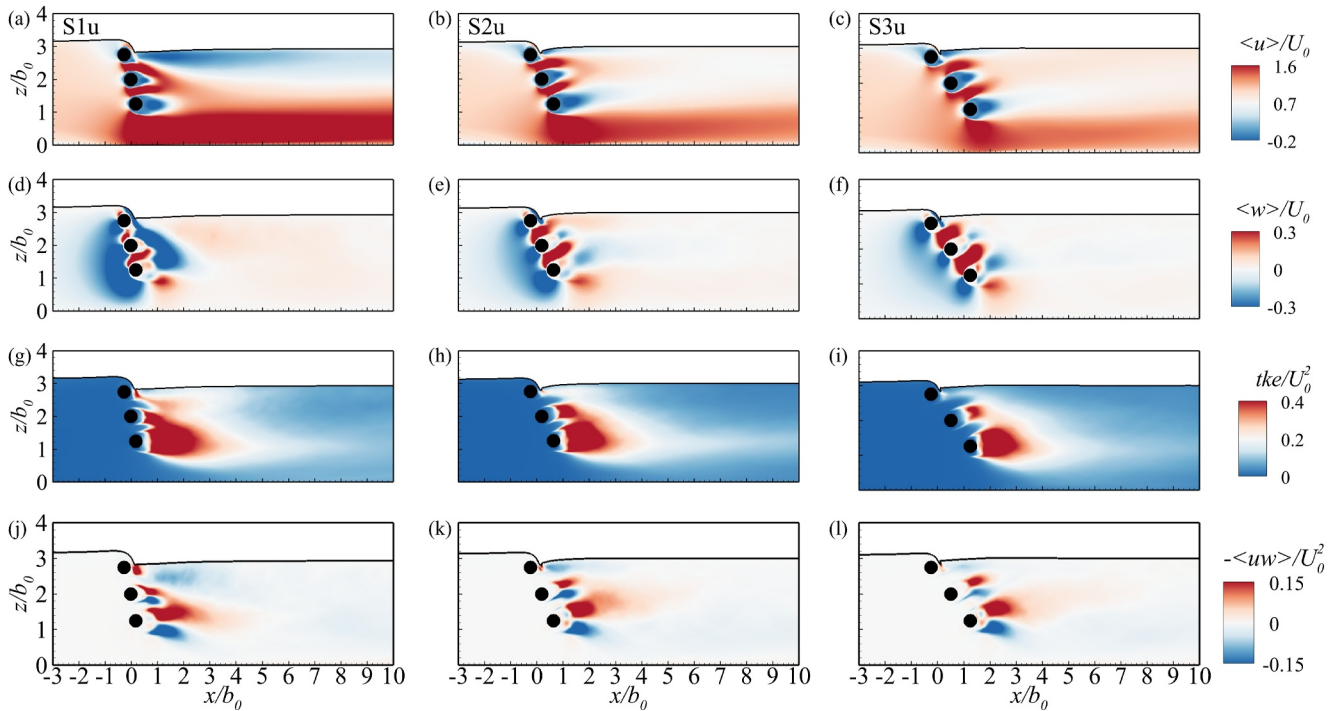


Figure 15. Side elevation contour plots of the LES computed (a–c) streamwise velocity, (d–f) vertical velocity, (g–i) turbulent kinetic energy, and (j–l) Reynolds shear stress, normalized by the bulk velocity for the upstream-inclined cases (S1u, S2u, and S3u).

compared to the other cases. This decrease originates from the redirection of flow through the inter-log gaps in an upwards direction, thereby limiting the influence of the formed secondary jets on the bottom region ($z/b_0 < 1$). In contrast to the downstream-inclined cases (Figures 14a–14c), in the upstream-inclined cases exhibit an increase in $\langle u \rangle$ as the barrier angle increases. Contour plots of the time-averaged vertical velocities (Figures 15d–15f) show that increasing the angle of the structure toward the upstream direction results in an upwards fluid motion through the inter-log gaps of the barrier.

Figures 15g–15i show that the upstream-inclined cases exhibit a highly turbulent wake, mainly along the heights of the middle and bottom logs, until $x/b_0 = 2$, followed by a region between $2 < x/b_0 < 6$, where turbulence decays. As the barrier angle increases toward the upstream direction, the magnitude of tke remains high. Figures 15j–15l show that, regardless of the barrier's angle, the distribution of the vertical Reynolds shear stress behind the lowermost logs remains consistent across the upstream designs with negligible differences in their shear stress magnitude.

3.4. Recirculation Region

The logs of the leaky barriers create recirculation zones of various scales immediately downstream, characterized by low streamwise velocities, as shown in Figure 16. The recirculation zone behind the top log exhibits just one recirculation core enclosed on the lower side of the log, while the upper recirculation core is affected by the proximity to the free surface and overtopping flow that plunges downstream of the log edge. In contrast, in the recirculation zones behind the other logs, both the upper and lower cores of the recirculation appearing almost symmetrical to the center of the logs.

Figure 16 shows that the recirculation zones exhibit a downwards inclination when the barrier is inclined in the downstream direction, while an upwards inclination can be observed with upstream-inclined barriers. The direction of the barrier inclination, along with the proximity effects of the adjacent logs, leads to variations in the length of the recirculation zones behind the logs. For instance, the mean recirculation length (L_r), which represents the distance from the endpoint of the log to the coordinate where the flow reattaches, is larger in the upstream cases compared to the downstream configurations. Differences of about 15% are observed between the 15° inclined cases (S1d and S1u), and differences exceeding 50% are seen in cases with higher angles. The L_r/b_0

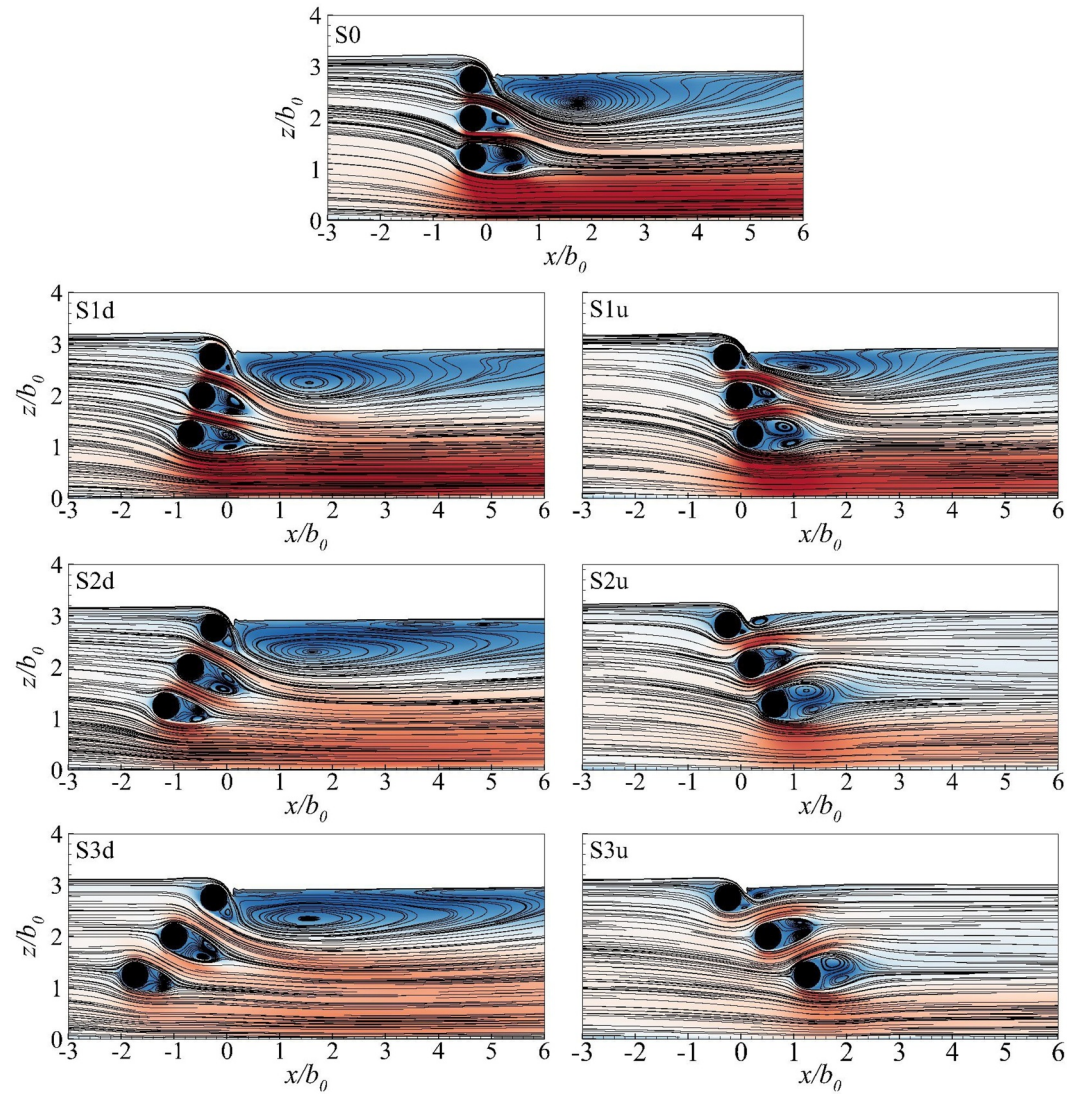


Figure 16. Comparison of the mean recirculation regions computed using LES for all simulated cases, with contours of the mean streamwise velocity normalized by the bulk velocity. Same legends as Figure 13a.

ratios are 0.91, 1.24, and 1.01 for the S1u, S2u, and S3u cases respectively, and 0.77, 0.52, and 0.50 for the S1d, S2d, and S3d cases, respectively.

The flow diverted through the inter-log gaps of the barrier toward the lower downstream region ($z/b_0 \leq 2.5$), creates a flow pattern that leads to an extended recirculation zone underneath the free surface, as shown in Figure 16 for the non-inclined case and the downstream-inclined cases. However, when the barrier is inclined upstream, the recirculation zone shrinks in the S1u case and nearly disappears in the S2u and S3u cases due to the upwards flow through the inter-log gaps, resulting in higher streamwise velocities near the free surface.

3.5. Recovery of Mean Streamwise Velocity

The velocity deficit in the streamwise direction, determined as $\left(\Delta\langle u \rangle = \frac{\langle u \rangle - \langle u \rangle_{x/b_0 = -10}}{\langle u \rangle_{x/b_0 = -10}}\right)$ between a selected far upstream station ($x/b_0 = -10$) and downstream profiles at $x/b_0 = 2-29$, is calculated to evaluate the influence of the structural design on wake recovery, as shown in Figure 17. All of the leaky barriers initially show a velocity surplus ($\Delta\langle u \rangle > 0$) along the bottom gap ($z/b_0 < 1$) due to the high-momentum flow exiting underneath the

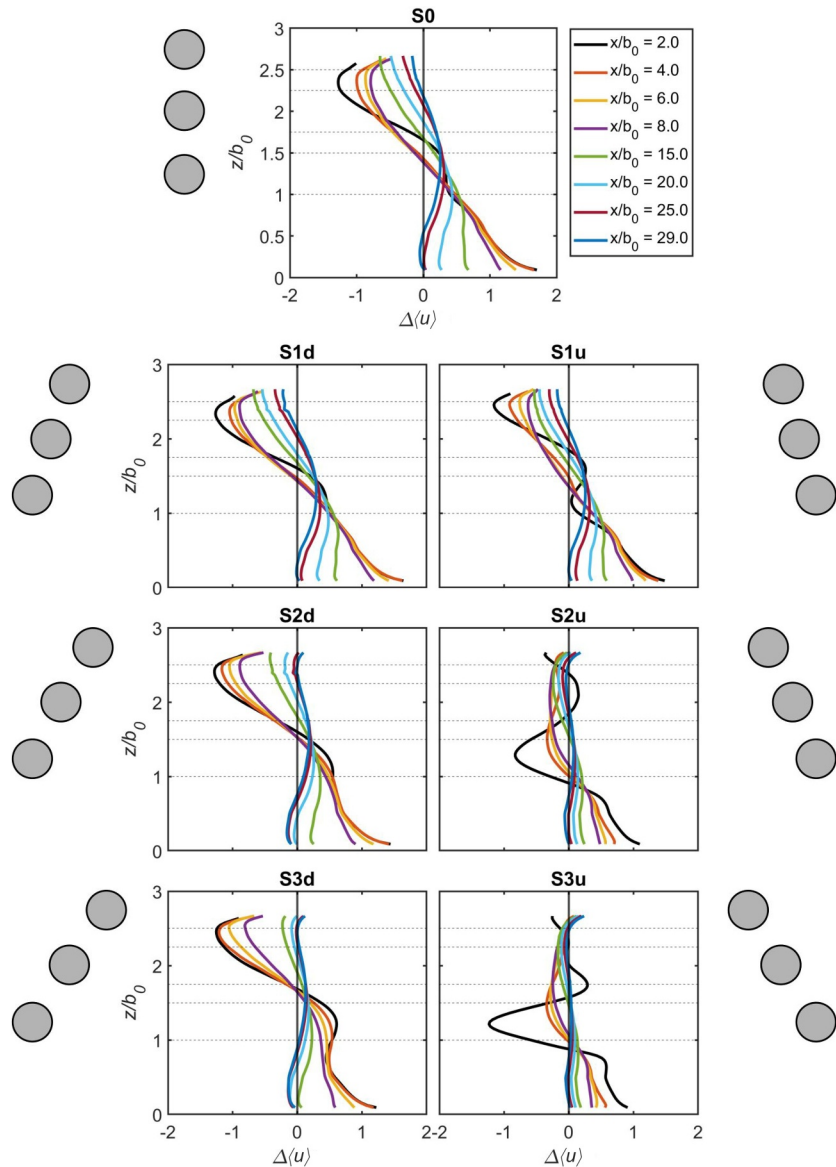


Figure 17. Vertical profiles of velocity deficit ($\Delta\langle u \rangle$) computed from the difference between the upstream profile ($x/b_0 = -10$) and selected downstream profiles for all of the simulated cases. The horizontal dashed lines indicate the logs positions. The solid vertical line indicates the zero-velocity deficit ($\Delta\langle u \rangle = 0$).

barriers. The S2u and S3u cases yield a more pronounced difference between the first downstream profile ($x/b_0 = 2$) and subsequent profiles, indicating a faster rate of wake recovery compared to the other cases.

In the upper wake region ($z/b_0 \approx 1.5 - 2.5$), all cases exhibit a velocity deficit ($\Delta\langle u \rangle < 0$) due to the wake of the leaky barrier, while for the S2u and S3u cases the deficit begins at a lower vertical height of $z/b_0 \approx 1$ (Figure 17). At $z/b_0 > 2$, the S0, S1d, and S1u cases show a similar pattern of $\Delta\langle u \rangle < 0$ in downstream profiles, suggesting that the streamwise velocity profile does not fully recover within the considered range for these cases as wake expands the longest. However, in the S2d case, wake recovery is mostly accomplished at $x/b_0 \geq 25$ with nearly zero-velocity deficit ($\Delta\langle u \rangle \approx 0$). The S3d design features a faster recovery in its wake, with negligible velocity deficit at $x/b_0 = 20$. In contrast, the upstream-inclined cases (S2u and S3u) exhibit a faster wake recovery closer to the barrier ($x/b_0 > 8$) throughout the water column (Figure 17).

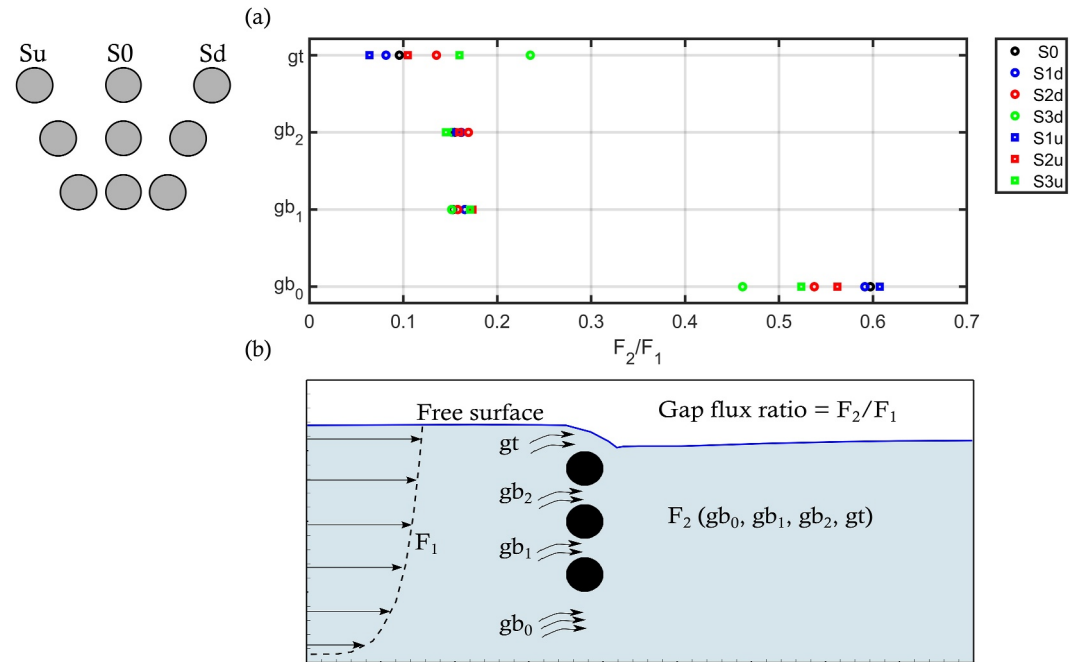


Figure 18. (a) The variation of the gap flux ratio (F_2/F_1) with gap position and barrier inclination. (b) Schematic diagram indicating the definition of the gap flux ratio and gap positions (gb_0 , gb_1 , gb_2 , gt) with F_1 representing the flux at $x/b_0 = -10$, while F_2 represents the flux at the different gap positions.

3.6. Gap Flow Ratio

The flow developed through barrier gaps significantly influences the downstream dynamics of the barrier. To gain a better understanding of the flow rate at each gap, an analysis of the time-averaged flow rate is conducted, focusing on calculating the gap flux ratio, based on the ratio between the flow rate through the gap (F_2) and incoming mean flow rate (F_1). Figure 18a presents how the gap flux ratio (F_2/F_1) correlates with the change in barrier inclination at each gap position. The F_1 calculations are performed between the mean free-surface level and the bottom wall, at $x/b_0 = -10$. For F_2 , the calculations are done vertically along each gap, including gb_0 (bottom), gb_1 (lower inter-log), gb_2 (upper inter-log) and gt (top between the top log and free surface), as illustrated in Figure 18b. The gap flux ratios at the bottom gap (gb_0) exhibit the highest values among all gaps, ranging approximately from $F_2/F_1 = 0.47$ to 0.61 . Conversely, the flux ratios at the inter-log gaps, gb_1 and gb_2 , show negligible differences between designs and contribute to an average total of 32% of flow passing through these gaps. Although variations in the flux ratios exist between cases at the top gap, the gap flux ratio is minimal compared to the ratios at the other positions, with a maximum of $F_2/F_1 = 0.24$ for the S3d case.

The flux ratio gb_0 decreases as the angle of the barrier increases in both upstream and downstream directions, with the reduction being greater for the downstream-inclined layouts. For instance, the flux ratio for the downstream designs reduces by approximately 22% from 0.59 for S1d to 0.46 for S3d, compared to a reduction of approximately 15% from 0.61 for S1u to 0.52 for S3u. The flux ratios of the bottom gap can be correlated with the initiation of the high-momentum jet formed beneath the structure, where a larger flux ratio indicates a stronger initiation of the jet, while a smaller flux ratio corresponds to a weaker jet. The minimal variations in the flux ratios at the inter-log gaps between the barriers can likely be attributed to their narrow width gaps, which are smaller than the bottom gap. This is anticipated to result in an analogous strength in the initiation of the offset jets across all cases.

Varying the angles of the barrier in both directions affects the elevation of the free surface at the top of the barrier. The flux ratios at the top gap are smaller than the values at gb_2 , except for the S3d and S3u cases, which exhibit larger flux ratios. The top-gap flux ratio reflects the proportion of incoming flow overtopping the barrier. The flux ratio at the top gap is inversely proportional to the flux ratio at the bottom gap for all inclined cases (Figure 18a).

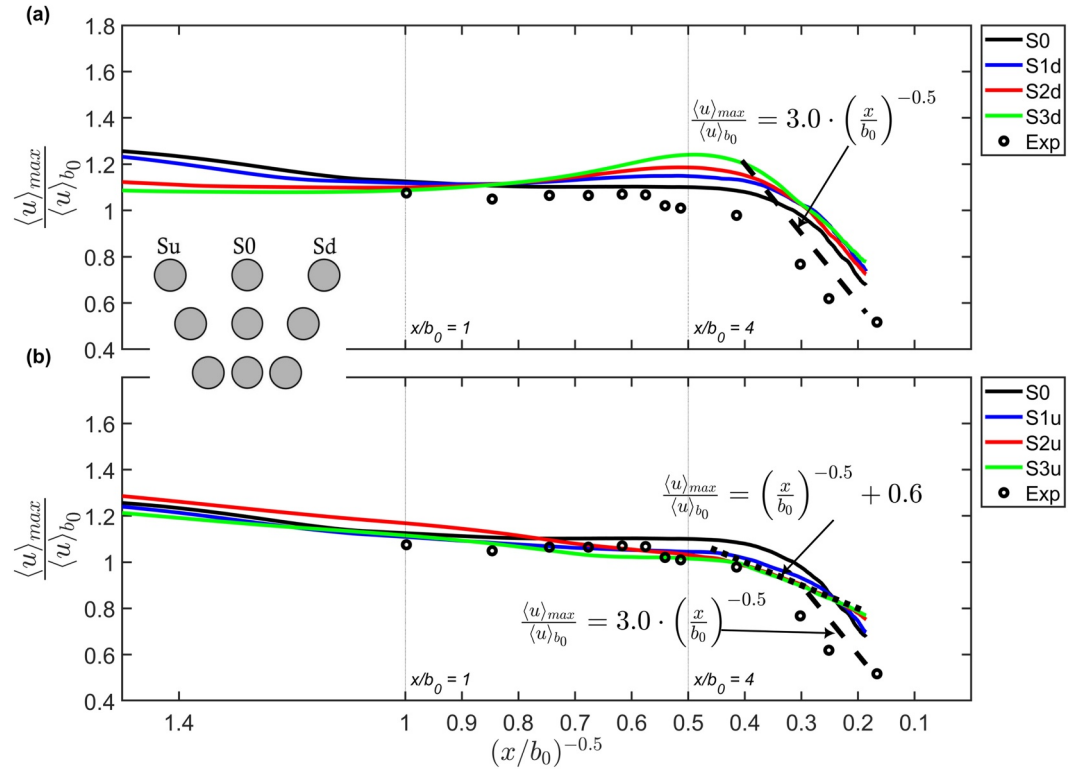


Figure 19. Decay of local maximum velocity $\langle u \rangle_{max}$ downstream of barriers relative to depth-averaged initial jet velocity $\langle u \rangle_{b_0}$ in the lower gap region ($0 \leq z/b_0 \leq 1$) with increasing longitudinal distance from the barrier $(x/b_0)^{-0.5}$. The vertical dotted line at $x/b_0 = 1$ denotes the initial downstream point where the average velocity over the bottom gap is calculated. The vertical dotted line at $x/b_0 = 4$ denotes the length of the potential core region, after which the maximum jet velocity experiences a similar decay pattern. The dashed black line indicates the rate of decay scaling with a decay coefficient of 3.0. The decay with a coefficient of 3 is shown as a dashed line, while the decay with a coefficient of 1 is represented by a dotted line.

3.7. Decay of the Maximum Jet Velocity

The maximum streamwise velocity ($\langle u \rangle_{max}$) varies in the downstream direction depending on the barrier's angle. Figure 19 shows the decay of $\langle u \rangle_{max} / \langle u \rangle_{b_0}$ in the longitudinal direction over the lower gap region ($0 \leq z/b_0 \leq 1$), which scales proportional to $C_{wj}(x/b_0)^{-0.5}$, where C_{wj} represents the decay coefficient of the wall jet (Wu & Rajaratnam, 1995). In the range of $1 < x/b_0 < 4$, there is no notable decay of the maximum jet velocity for the vertical barrier, S0, based on both LES and experimental results (Müller et al., 2021a, 2021b). Ead and Rajaratnam (2002) defined this region ($1 < x/b_0 < 4$) as the potential core region, where the maximum jet velocity remains close to the initial value. For the downstream-inclined barriers (S1d, S2d, S3d) and non-inclined barrier (S0) (Figure 19a), the decay of normalized maximum velocity follows the scaling law $\langle u \rangle_{max} / \langle u \rangle_{b_0} = 3.0(x/b_0)^{-0.5}$ for the range $(x/b_0)^{-0.5} < 0.4$, that is, for $x/b_0 > 4$. For the upstream-inclined barriers (S1u, S2u, S3u) (Figure 19b), the decay behavior changes compared to the downstream-inclined cases as flow underneath the leaky barrier varies. In the range of $(x/b_0)^{-0.5}$ between 0.45 and 0.15, the maximum normalized velocity decay follows a $(x/b_0)^{-0.5} + 0.6$ slope decay, which indicates that the velocity reduces at a slower rate. For $(x/b_0)^{-0.5} < 0.25$, the decay coefficient of 3.0 is still suitable for the S1u design.

3.8. Bed Shear Stress

The increase in near-bed velocity in the vicinity of a leaky barrier is likely to enhance bed shear stress, thereby increasing the risk of local scour and sediment mobilization (Beebe, 2000; Lagasse et al., 2010). This process can be further exacerbated by the upstream vertical flow diversion and the resultant high-momentum flow beneath the barrier. Bed shear stress ($\tau_w = \mu(\partial \langle u \rangle / \partial z)$) is determined from the first grid cell of the bottom wall

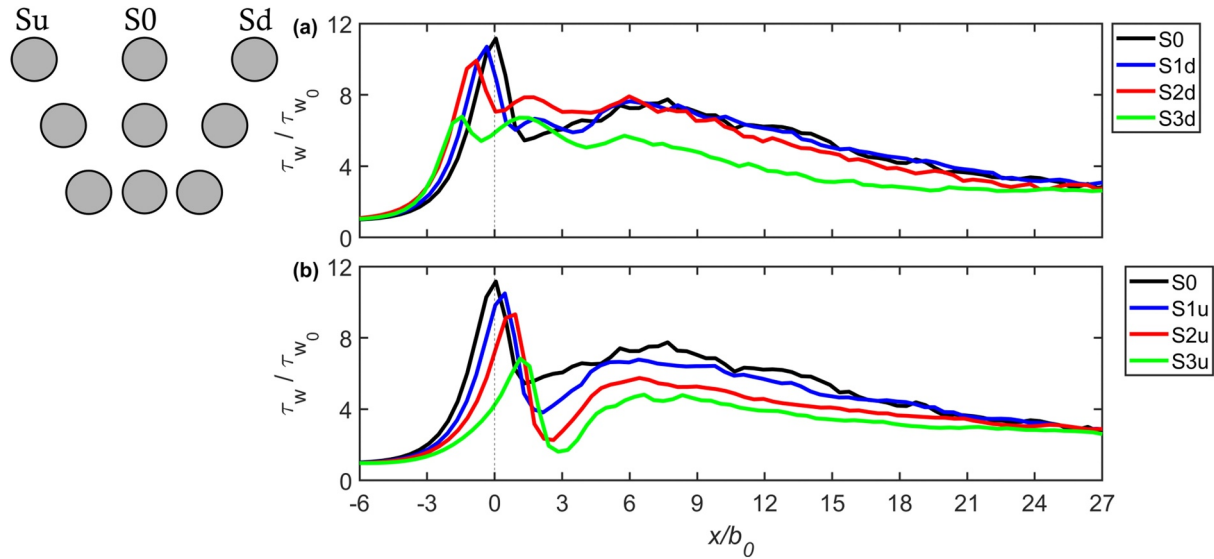


Figure 20. Comparison of the bed shear stress τ_w , normalized by an initial bed shear stress τ_{w0} ($x/b_0 = -6$) for (a) the downstream inclined barriers and (b) the upstream inclined barriers, including the values of the non-inclined barrier (S0). The vertical dashed line at $x/b_0 = 0$ denotes the origin of the x -coordinates, which represents the downstream edge of the top log in all cases.

($z/b_0 = 0.0125$) for all cases, as presented in Figure 20. In the vicinity of the barrier, $-2 < x/b_0 < 2$, the maximum bed shear stress increases with decreasing barrier angle in either direction and being maximum for the S0 layout. Peaks in τ_w relative to an initial bed shear stress τ_{w0} , which is considered at a specific point located far upstream of the barrier ($x/b_0 = -6$), are found at x/b_0 values of 0.05, -0.34 , -0.81 , -1.44 , 0.45, 0.91, and 1.12 for the S0, S1d, S2d, S3d, S1u, S2u, and S3u cases respectively, yielding values of $\tau_w/\tau_{w0} = 11.2, 10.6, 10.0, 6.8, 10.5, 9.3,$ and 6.7 , for these designs. For all cases, the peak in bed shear stress is observed approximately around the streamwise position of the lowest log. Regardless of the direction of barrier inclination, there are slight variations in the maxima of τ_w between cases with the same angle, that is, S1d and S1u.

For the upstream configurations, the distribution of τ_w/τ_{w0} indicates a marked decrease in bed shear stress magnitude immediately downstream of the barrier for all cases (Figure 20b), for example, at $x/b_0 \approx 3$ for the S3u configuration. Moreover, as the streamwise distance from the barrier increases, there is a subsequent additional rise in τ_w/τ_{w0} , with a peak at downstream location $x/b_0 \approx 6 - 9$. This increase is observed in the region where the secondary jets can interact with the main wall jet (Figure 15), and this behavior is attenuated for the barriers with a flatter layout. Further downstream from this location, all cases exhibit a gradual decrease until they converge to an approximate value of $\tau_w/\tau_{w0} = 2.8$ at around $x/b_0 = 27$.

Alluvial rivers can be broadly categorized into two types based on the median diameter of their sediment particles (d_{50}). Sand-bed streams typically have a d_{50} ranging from 0.0625 to 2 mm, whilst gravel-bed streams range from 2 to 64 mm (Bunte, 2001; Hey & Thorne, 1986). In this context, a scale for natural-flood management streams was established using a model-to-prototype ratio of 1:10, which was derived from the geometric scaling of bankfull depth and log diameter. Specifically, geometric scaling involves preserving certain geometric properties between the model and the prototype. In this case, the 1:10 scale ratio was chosen to ensure that the bankfull depth and log diameter in the model are 1/10th of those in the prototype, maintaining geometric similarity between the two systems. Following sediment transport scaling guidelines (Pugh, 2008), the sand grain sizes were adjusted to conform to Froude scaling, ensuring a settling velocity consistent with the Froude law. For prototype values of d_{50} ranging from 8 to 14 mm, the corresponding model values, utilizing a 1:10 model-to-prototype scaling, fall within the range of 0.8–1.4 mm. These values are utilized in the calculation of the Shields parameter, which serves as an indicator of sediment movement.

Figure 21 presents profiles of bed shear stress normalized by the critical bed shear stress, $\tau_c = \rho u_{*c}^2$, where, u_{*c} represents the critical shear velocity required to initiate sediment motion, which is determined based on d_{50}

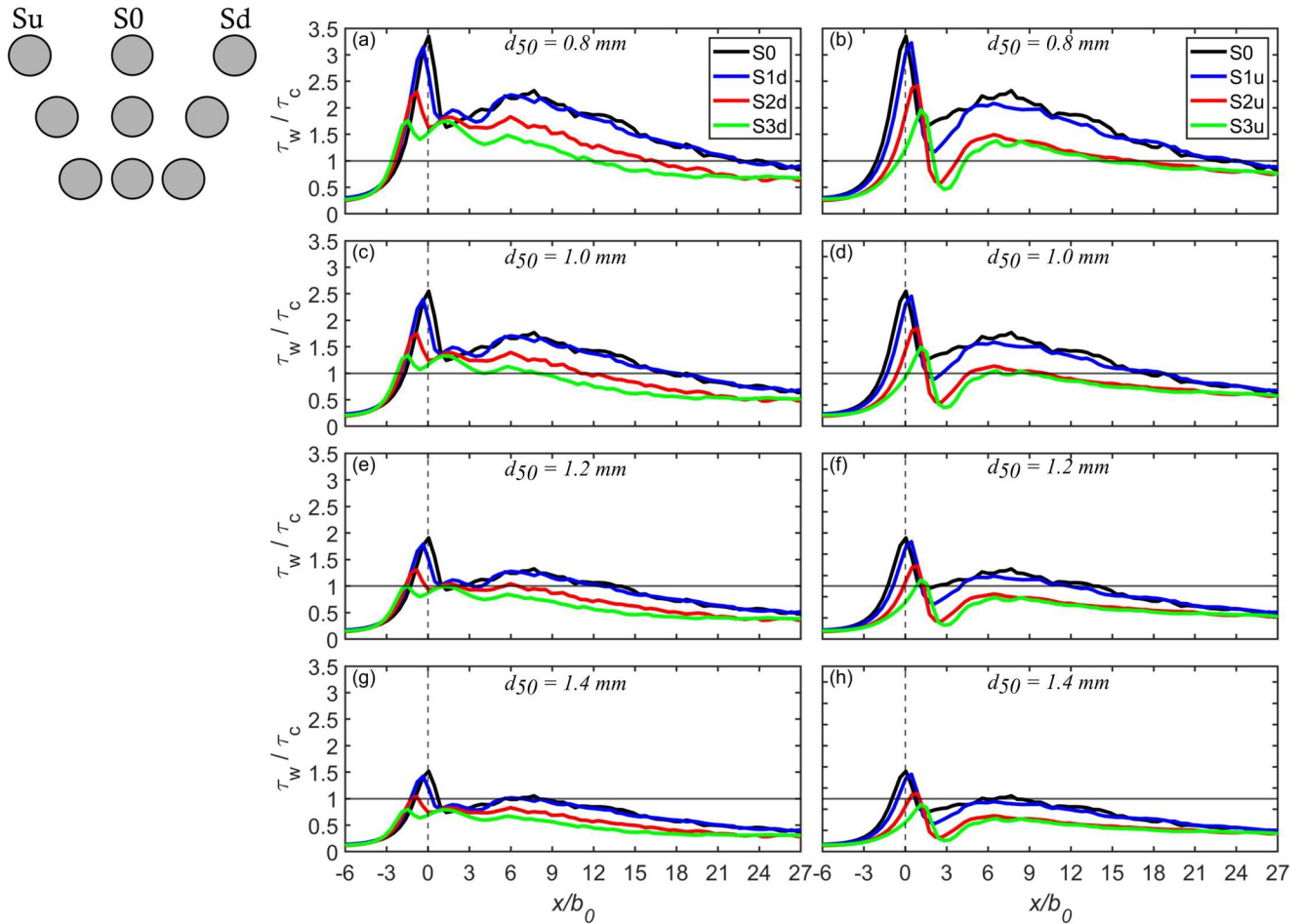


Figure 21. Normalized bed shear stress profiles for the vertical and the inclined barriers to the upstream and downstream directions at (a and b) $d_{50} = 0.8$ mm, (c and d) $d_{50} = 1.0$ mm, (e and f) $d_{50} = 1.2$ mm and (g and h) $d_{50} = 1.4$ mm. The horizontal black line is the threshold line of motion, where $\tau_w/\tau_c > 1$ depicts possible sediment motion. The vertical dashed line is the origin of the x coordinates, which represents the downstream edge of the top log in all cases.

(Julien, 1995). Zones where $\tau_w/\tau_c > 1$ are indicative of potential sediment entrainment activities. The smallest sediment size ($d_{50} = 0.8$ mm) exhibits the largest scour pool length and potential scour depth (Figures 21a and 21b). As the sediment size increases, the longitudinal extent of the scouring decreases and is solely in the vicinity of the structure ($-2 < x/b_0 < 2$), as seen in Figures 21c–21h. With the increase in the angle of barrier in either direction, the longitudinal extent of the downstream region susceptible to sediment motion ($\tau_w/\tau_c > 1$) reduces. For a sediment size of $d_{50} = 0.8$ mm, the downstream region prone to sediment motion extends up to $x/b_0 = 23$ in the S0 case. However, for the flattest inclination in the downstream direction (S3d), this extent is shortened to $x/b_0 = 13$. This trend of reduced longitudinal extent of sediment motion continues as the sediment size increases. For S3d and S3u cases with $d_{50} = 1.4$ mm, no bed erosion will occur, while all other cases will exhibit limited bed erosion (Figures 21g and 21h).

Scour length (L_{sc}) is determined when the bed shear stress exceed the values of the critical shear stress. Figure 22 presents the calculated scour length for four distinct sediment particle diameters, each with a confidence interval of 10%. The 10% margin was chosen based on uncertainties in the selection of the Shields parameter. The original Shields diagram exhibits a clear range of variation, illustrating the variability in critical shear stress values necessary for the incipient motion of sediment particles (Shields, 1936). Several factors contribute to this variability, including grain size, bedform features, flow properties, bed roughness, and channel gradient (Buffington & Montgomery, 1997; Church et al., 1998; Shields, 1936; Shvidchenko & Pender, 2000). Moreover, in this study, when employing the velocity gradient method to calculate bed shear stress, the one-dimensional nature of the

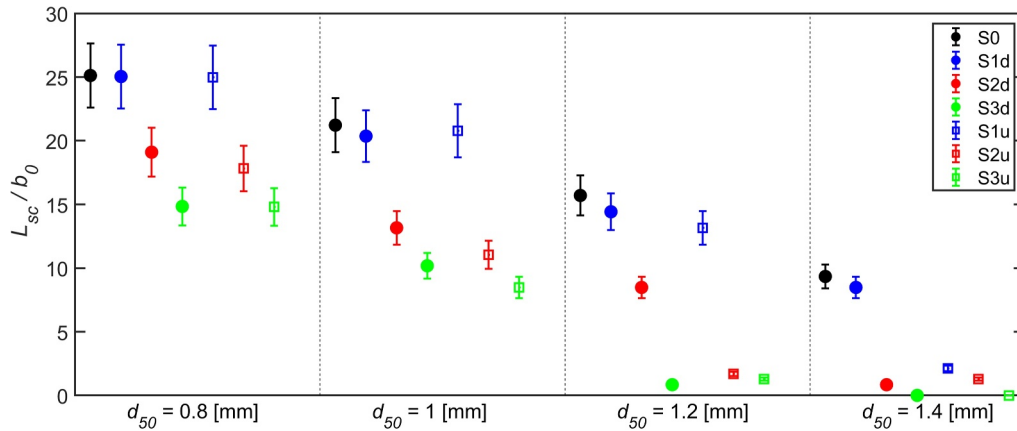


Figure 22. Plot of the estimated scour length normalized by the bottom gap height (L_{sc}/b_0) for the simulated cases considering four different sizes of sediment particle diameter ($d_{50} = 0.8, 1.0, 1.2,$ and 1.4 mm), plotted with a confidence interval of 10%.

approach can pose challenges in determining an accurate average bed shear stress, given that flows are inherently three-dimensional.

The finest sediment with a $d_{50} = 0.8$ mm exhibits the greatest scour length, which decreases as the d_{50} value increases. For instance, the non-inclined barrier has an estimated scour length of approximately 1.3 m for a sediment size of $d_{50} = 0.8$ mm, decreasing to about 0.5 m for $d_{50} = 1.4$ mm. In general, the increase in the angle of barrier in either direction results in smaller scour lengths, with the upstream-inclined barriers exhibiting the smallest values. For instance, at $d_{50} = 1$ mm, differences in scour lengths are noted between S2u, S3u versus S2d, and S3d, with the latter two being greater. However, the S3d and S3u cases exhibit no scour development at $d_{50} = 1.4$ mm.

3.9. Hydrodynamic Coefficients

The hydrodynamic forces experienced by the logs are influenced by the presence of an asymmetric flow field that develops around them, a consequence of the logs' proximity to each other, their closeness to the bottom wall and the free-surface layer, as well as the logarithmic distribution of upstream velocity. The forces acting on the logs, namely in the horizontal (F_x) and vertical (F_z) directions, are directly calculated using the forces obtained from the immersed boundary method. These forces are then employed to calculate the drag (C_D) and lift (C_L) coefficients as follows:

$$C_D = \frac{F_x}{1/2\rho AU_0^2}, \quad C_L = \frac{F_z}{1/2\rho AU_0^2} \quad (11)$$

where ρ is the fluid density and A is the cross-sectional area of the log, which is determined by multiplying the width of the computational domain B and the log's diameter D .

The drag and lift coefficients are determined for each barrier log in all layouts and presented in Figure 23. The average drag coefficients on the top, middle and bottom logs are the largest for the non-inclined barrier, with values of $C_D = 2.1, 2.2$ and 1.7 respectively. These values decrease as the angle of the barrier increases in either direction (Figure 23a). However, the differences in the mean drag coefficients on all logs between the inclined-upstream and inclined-downstream cases are small, showing a maximum difference of 16% between S2d and S2u. For the S0, S1d, S1u, and S2u cases, the mean drag coefficients on the middle log are larger than those on the other logs, whereas for the S3d and S3u layouts the top logs experience the largest drag force. For the S2d case, the mean drag coefficients on all logs are similar. In all cases, the bottom log consistently exhibits smaller drag coefficients compared to the other logs. This is due to the fact that the blockage effect is larger for the top and middle logs than for the bottom logs. In addition, the top and middle logs are influenced by both the free surface and the secondary jets, affecting the separation of the shear layers behind them. This, in turn, leads to an

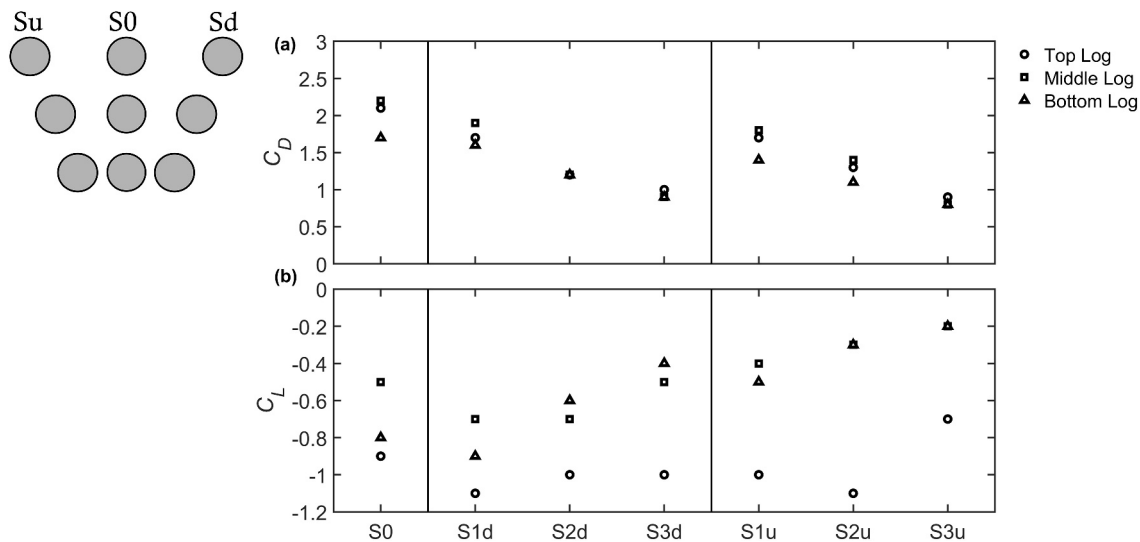


Figure 23. Time-averaged (a) drag (C_D) and (b) lift (C_L) coefficients of the top, middle and bottom logs for all the simulated leaky barriers.

asymmetric pressure distribution around the logs, and consequently an increase in their drag coefficient (Chu et al., 2018).

Figure 23b reveals that with the close placement of the top log to the free surface, the lift coefficients in all cases reach their maximum value compared to those at the other logs, indicating a downward force on the top log ranging from $C_L = -0.7$ to -1.1 . For the S0, S1d, and S1u configurations, the lift coefficients on the middle log are smaller than those on the other logs, attributed to the shielding effect from the other logs (Tong et al., 2015). With the increase of barrier angle, there is a reduction of the shielding effect, showing smaller lift coefficients on the bottom log than that on the middle one. However, for the S2u and S3u cases, there are no differences in the lift coefficients between the middle and bottom logs, with mean values of $C_L = -0.3$ and -0.2 , respectively. When comparing the upstream and downstream-inclined cases, there are larger lift coefficients on the middle and bottom cylinders due to increased downward force in the downstream-inclined designs. This discrepancy suggests that in the upstream-inclined cases, there is resistance to the downwards thrust on these logs as the flow through the structure is diverted toward the free surface due to the direction of barrier inclination.

4. Leaky Barrier Design: Performance Evaluation From an Integral Hydrodynamic Perspective

The seven simulated leaky barrier configurations are assessed based on five identified performance aspects. The first aspect to be evaluated is backwater rise, which is a key consideration for well-designed leaky barriers, because this aims to improve channel-floodplain connectivity and water storage, and promote infiltration into the ground (Collins et al., 2012; Muhawenimana et al., 2023; Schalko et al., 2019). The second aspect to be evaluated in barrier design is to achieve a faster wake recovery, which reduces potential disturbances to aquatic environments or structures, that is, additional barriers or infrastructure (Bisson & Vvondzei, 2003; Müller et al., 2022; Reich, 2003). The third performance criterion is the extent of recirculation occurring near the free surface, which induces turbulence and can challenge local aquatic fauna by hindering fish navigation and obstructing migratory patterns (Castro-Santos, 2005). This turbulence can also lead to lateral bank erosion, posing risks of instability and potential failure, particularly for unprotected or unvegetated banks (Zhang et al., 2020). The fourth aspect to consider is the potential for bed scour. A proper design of a leaky barrier should prioritize minimizing scouring because this alters the surrounding channel hydrodynamics and bank morphology (Dixon & Sear, 2014; Wohl & Iskin, 2022). Finally, leaky barrier design should also focus on limiting the magnitude of the total force exerted on logs because this is essential for maintaining the barrier's structural integrity under varying hydrodynamic conditions (Gippel et al., 1996).

Table 2 presents an evaluation of the seven leaky barrier configurations, assessed across these five key design criteria: backwater rise (Figure 4), recirculation adjacent to the free surface (Figure 16), wake recovery

Table 2
Performance Evaluation of Leaky Barrier Configurations According to a Variety of Design Criteria

LB design	Backwater rise	Wake recovery	Recirculation adjacent to free surface	Potential bed scour	Structural loads on logs	Total
S0	5	3	2	1	1	12
S1u	4	4	3	2	2	15
S2u	3	5	4	4	3	19
S3u	2	5	4	5	5	21
S1d	5	3	2	1	2	13
S2d	3	4	1	3	4	15
S3d	2	4	1	5	5	17

Note. The rating of the design criteria is: 1 = Limited, 2 = Poor, 3 = Good, 4 = Very Good, and 5 = Excellent.

(Figure 17), potential bed scour (Figures 20–22), and structural load on logs (Figure 23). The scores for each criterion range from one to five, with five indicating the best performance. Configurations S0 and S1d score five in backwater rise, but S0 achieves a total low score of 12, which indicates suboptimal performance in other categories, whereas the S1d configuration obtains a slightly higher total score of 13, which is primarily due to a diminished structural load on the logs. Both the S1u and S2d barriers yield a total score of 15, with their performance varying across individual criteria. For instance, S1u scores four out of five in backwater rise and wake recovery, despite showing a lower performance in other aspects. Meanwhile, S2d achieves a rating of four (out of five) in wake recovery and structural load on logs and a three in backwater rise.

The scoring system is qualitative and based on a single, steady-state hydrodynamic inflow condition, reflecting a simplified comparison of performance and not for peak flood discharge. With a total score of 19, the S2u case achieves a score of 5 in wake recovery and 4 in both recirculation adjacent to the free surface and potential bed scour, significantly contributing to its overall performance. In comparison to the S2u design, the S3u configuration improves the performance in bed shear stress and structural loads but induces less backwater rise, ultimately achieving the highest mark of 21. Despite the lower total score of 17 for the S3d configuration compared to S3u, it scores 5 in potential bed scour and structural load on logs, which is similar to the rating to the S3u design.

The flow conditions used in the study are representative of idealized simulations, but further studies under unsteady flow conditions would be necessary to better capture real-world flood dynamics. Overall, the upstream-inclined configurations outperform their downstream counterparts, particularly those with flatter inclinations such as the S3u design. Consequently, when assessing the effect of leaky barrier design, it is clear that when a leaky barrier is designed to achieve maximum backwater rise, this leads to a decreased performance in the other essential criteria, and vice versa.

5. Conclusion

Flow around leaky barriers (LB) composed of three cylindrical logs was investigated using large-eddy simulation. The main LB configuration considered vertically aligned logs, with other layouts inclined at $\gamma = 15^\circ, 30^\circ,$ and 45° in both upstream and downstream directions. The simulations were conducted at a bulk Reynolds number of 43,500 based on the cylinder's diameter and mean water depth, and for when the barrier crest is submerged. The LES results were validated for the main configuration where logs were vertically aligned (S0), showing good agreement with the experimental results for time-averaged flow quantities and free surface elevation. The simulation successfully captured the streamwise and vertical velocities, their time-averaged fluctuations, and variation in the free surface layer and high-momentum jet underneath the barrier.

For all barrier configurations, the close proximity of the upper log to the free surface impacts the upper shear layers, which deflect downwards interacting with the shear layers generated from the adjacent mid log, increasing the unsteadiness and coherence of the log's turbulent wake. Increasing the angle of the barrier toward the upstream direction resulted in reduced longitudinal extent of the wake regions with high streamwise velocities along the bottom gap and increased streamwise velocities in downstream regions near the free surface compared to the other cases. In addition, upstream-inclined barrier designs (S1u, S2u, S3u) resulted in high upward velocities through the inter-log gaps of the barrier. This is in contrast to the downstream-inclined designs (S1d, S2d, S3d), where

vortices traveled predominantly downwards toward the bottom bed. Increasing the barrier's orientation angle in the downstream direction reduced both turbulent kinetic energy and vertical Reynolds shear stress.

The inclination of the barriers significantly impacted the flow dynamics, with implications on the formation of recirculation zones downstream of the leaky barrier, wake recovery, and the gap flux ratio. Both vertically aligned and downstream-inclined barriers developed a large recirculation zone near the free surface. However, upstream inclination of the barrier, particularly in the S2u and S3u cases, limited the formation of this recirculation zone. Barrier designs with flatter inclinations upstream (S3u) demonstrated quicker wake recovery and an earlier return to near-zero velocity deficit in the far wake compared to cases with greater angles in the downstream direction. Variations in the gap flux ratio revealed that flattening the barrier inclination in both directions (S3u, S3d) resulted in differences in the fluxes at the bottom gap and between the upper log and the free surface, while negligible differences were found in the inter-log gap fluxes.

In assessing how leaky barrier design influenced bed shear stress, flatter barrier designs (S3u, S3d) resulted in a decrease in peak bed shear stress, effectively diminishing the scour potential and reducing the scouring pool region underneath the barrier and immediately downstream. The structural load on the logs was influenced by the log configuration, and as the logs were arranged in a flatter configuration (angle increased), the drag and lift coefficients decreased. The top log exhibited a larger downward force compared to the other logs due to its proximity to the free surface.

This study's findings give new insight into leaky barrier hydrodynamics and barrier design. Our results indicate that to maximize backwater rise a leaky barrier design with logs aligned in the vertical plane is advantageous to an inclined design. If the risk of local bed and bank scouring needs to be limited and considered in light of site sediment management goals and site-specific conditions (e.g., steep bed slope) then scour risk can be mitigated by the utilization of an upstream- or downstream-inclined barrier design. To achieve a balance between optimal flood mitigation and sediment management, an upstream-inclined configuration offers the best hydrodynamic performance. In natural flood management schemes consideration needs to be given to a strategy that integrates aspects of these design elements in working toward sustainable solutions which are sensitive to the stream and catchment setting. Further research is necessary to explore the comprehensive impact of various factors on barrier performance. Future studies could investigate the interplay between barrier angle and other critical parameters such as flow depth, interspace between logs, number of logs, and sediment transport characteristics. In addition, the effect of varying hydraulic and morphological conditions on the efficacy and environmental compatibility of leaky barriers warrants detailed examination. Understanding these dynamics can significantly contribute to the development of more effective and environmentally sensitive flood management strategies.

Data Availability Statement

The simulation data presented in this paper can be downloaded from Alzabari et al. (2024). The software adopted to analyse results and process figures are Tecplot Focus version 2021 R2 (<https://tecplot.com/products/tecplot-focus/>).

References

- Adzic, F., Stoesser, T., Liu, Y., & Xie, Z. (2022). Large-eddy simulation of supercritical free-surface flow in an open-channel contraction. *Journal of Hydraulic Research*, 60(4), 628–644. <https://doi.org/10.1080/00221686.2022.2041496>
- Alam, M. M. (2014). The aerodynamics of a cylinder submerged in the wake of another. *Journal of Fluids and Structures*, 51, 393–400. <https://doi.org/10.1016/j.jfluidstructs.2014.08.003>
- Alam, M. M., & Meyer, J. P. (2013). Global aerodynamic instability of twin cylinders in cross flow. *Journal of Fluids and Structures*, 41, 135–145. <https://doi.org/10.1016/j.jfluidstructs.2013.03.007>
- Alam, M. M., Moriya, M., & Sakamoto, H. (2003). Aerodynamic characteristics of two side-by-side circular cylinders and application of wavelet analysis on the switching phenomenon. *Journal of Fluids and Structures*, 18, 325–346.
- Altmann, M., Vanzo, D., Valero, D., & Schalko, I. (2024). A simple approach to simulate logjams in two-dimensional hydrodynamic models. *Journal of Hydraulic Engineering*, 150(4), 06024002. <https://doi.org/10.1061/jhend8.hyeng-13713>
- Alzabari, F., Wilson, C., & Ouro, P. (2024). Results files for hydrodynamics of in-stream leaky barriers for natural flood management. *Figshare*. <https://doi.org/10.6084/m9.figshare.27620196>
- Alzabari, F., Wilson, C. A., & Ouro, P. (2023). Unsteady vortex shedding dynamics behind a circular cylinder in very shallow free-surface flows. *Computers and Fluids*, 260, 105918. <https://doi.org/10.1016/j.compfluid.2023.105918>
- Beebe, J. (2000). Flume studies of the effect of perpendicular log obstruction on flow patterns and bed topography. *Great Lakes Geographer*, 7(1), 9–25.
- Bisson, P., & Vvondzei, S. M. (2003). Trends in using wood to restore aquatic habitats. *American Fisheries Society Symposium*, 37, 391–406.

Acknowledgments

The authors gratefully acknowledge the help of the Supercomputing Wales project, which is partially sponsored by the European Regional Development Fund (ERDF) via the Welsh Government.

- Bomminayuni, S., & Stoesser, T. (2011). Turbulence statistics in an open-channel flow over a rough bed. *Journal of Hydraulic Engineering*, 137(11), 1347–1358. [https://doi.org/10.1061/\(asce\)hy.1943-7900.0000454](https://doi.org/10.1061/(asce)hy.1943-7900.0000454)
- Bouscasse, B., Colagrossi, A., Marrone, S., & Souto-Iglesias, A. (2017). SPH modelling of viscous flow past a circular cylinder interacting with a free surface. *Computers & Fluids*, 16, 190–212. <https://doi.org/10.1016/j.compfluid.2017.01.011>
- Bouwes, N., Weber, N., Jordan, C. E., Saunders, W. C., Tattam, I. A., Volk, C., et al. (2016). Ecosystem experiment reveals benefits of natural and simulated beaver dams to a threatened population of steelhead (*Oncorhynchus mykiss*). *Scientific Reports*, 6(1), 28581. <https://doi.org/10.1038/srep28581>
- Bridges, T. S., Bourne, E. M., Suedel, B. C., Moynihan, E. B., & King, J. K. (2018). *Engineering with nature: An atlas*. US Army Engineer Research and Development Center, Environmental Laboratory.
- Buffington, J. M., & Montgomery, D. R. (1997). A systematic analysis of eight decades of incipient motion studies, with special reference to gravel-bedded rivers. *Water Resources Research*, 33(8), 1993–2029. <https://doi.org/10.1029/96wr03190>
- Bunte, K. (2001). *Sampling surface and subsurface particle-size distributions in wadable gravel-and cobble-bed streams for analyses in sediment transport, hydraulics, and streambed monitoring*. US Department of Agriculture, Forest Service, Rocky Mountain Research Station.
- Burgess-Gamble, L., Ngai, R., Wilkinson, M., Nisbet, T., Pontee, N., Harvey, R., et al. (2017). *Working with natural processes—evidence directory* Report No. SC150005. Environmental Agency.
- Bussmann, M., Chandra, S., & Mostaghimi, J. (2000). Modeling the splash of a droplet impacting a solid surface. *Physics of Fluids*, 12(12), 3121–3132. <https://doi.org/10.1063/1.1321258>
- Carberry, J. (2002). *Wake states of a submerged oscillating cylinder and of a cylinder beneath a free surface* (Unpublished doctoral dissertation). Monash University.
- Castro-Santos, T. (2005). Optimal swim speeds for traversing velocity barriers: An analysis of volitional high-speed swimming behavior of migratory fishes. *Journal of Experimental Biology*, 208(3), 421–432. <https://doi.org/10.1242/jeb.01380>
- Chen, W., Ji, C., Xu, D., An, H., & Zhang, Z. (2020). Flow-induced vibrations of two side-by-side circular cylinders at low Reynolds numbers. *Physics of Fluids*, 32(2), 023601. <https://doi.org/10.1063/1.5129013>
- Christou, A., Stoesser, T., & Xie, Z. (2021). A large-eddy-simulation-based numerical wave tank for three-dimensional wave-structure interaction. *Computers & Fluids*, 231, 105179. <https://doi.org/10.1016/j.compfluid.2021.105179>
- Christou, A., Xie, Z., Stoesser, T., & Ouro, P. (2021). Propagation of a solitary wave over a finite submerged thin plate. *Applied Ocean Research*, 106, 102425. <https://doi.org/10.1016/j.apor.2020.102425>
- Chu, C., Lin, Y.-A., Wu, T.-R., & Wang, C.-Y. (2018). Hydrodynamic force of a circular cylinder close to the water surface. *Computers and Fluids*, 171, 154–165. <https://doi.org/10.1016/j.compfluid.2018.05.032>
- Church, M., Hassan, M. A., & Wolcott, J. F. (1998). Stabilizing self-organized structures in gravel-bed stream channels: Field and experimental observations. *Water Resources Research*, 34(11), 3169–3179. <https://doi.org/10.1029/98wr00484>
- Collins, B. D., Montgomery, D. R., Fetherston, K. L., & Abbe, T. B. (2012). The floodplain large-wood cycle hypothesis: A mechanism for the physical and biotic structuring of temperate forested alluvial valleys in the north pacific coastal ecoregion. *Geomorphology*, 139, 460–470. <https://doi.org/10.1016/j.geomorph.2011.11.011>
- Dadson, S. J., Hall, J. W., Murgatroyd, A., Acreman, M., Bates, P., Beven, K., et al. (2017). A restatement of the natural science evidence concerning catchment-based “natural” flood management in the UK. *Proceedings of the Royal Society A: Mathematical, Physical and Engineering Sciences*, 473(2199), 20160706. <https://doi.org/10.1098/rspa.2016.0706>
- Dixon, S. J., & Sear, D. A. (2014). The influence of geomorphology on large wood dynamics in a low gradient headwater stream. *Water Resources Research*, 50(12), 9194–9210. <https://doi.org/10.1002/2014wr015947>
- Dodd, J., Newton, M., & Adams, C. (2016). The effect of natural flood management in-stream wood placements on fish movement in Scotland Report CD2015, 2.
- Ead, S., & Rajaratnam, N. (2002). Plane turbulent wall jets in shallow tailwater. *Journal of Engineering Mechanics*, 128(2), 143–155. [https://doi.org/10.1061/\(asce\)0733-9399\(2002\)128:2\(143\)](https://doi.org/10.1061/(asce)0733-9399(2002)128:2(143))
- Fischedick, M., Roy, J., Acquaye, A., Allwood, J., Ceron, J.-P., Geng, Y., et al. (2014). *Industry in: Climate change 2014: Mitigation of climate change. Contribution of working group III to the fifth assessment report of the intergovernmental panel on climate change* Technical Report. (Tech. Rep.). Cambridge University.
- Follett, E., & Wilson, C. (2020). Bedload sediment transport induced by channel-spanning instream structures. In *River flow 2020* (pp. 735–742). CRC Press.
- Gippel, C. J., O’Neill, I. C., Finlayson, B. L., & Schnatz, I. (1996). Hydraulic guidelines for the re-introduction and management of large woody debris in lowland rivers. *Regulated Rivers: Research and Management*, 12(2–3), 223–236. [https://doi.org/10.1002/\(sici\)1099-1646\(199603\)12:2/3<223::aid-rrr391>3.3.co;2-r](https://doi.org/10.1002/(sici)1099-1646(199603)12:2/3<223::aid-rrr391>3.3.co;2-r)
- Griffith, M., Jacono, D., Sheridan, J., & Leontini, J. (2017). Flow-induced vibration of two cylinders in tandem and staggered arrangements. *Journal of Fluid Mechanics*, 833, 98–130. <https://doi.org/10.1017/jfm.2017.673>
- Harichandan, A. B., & Roy, A. (2010). Numerical investigation of low Reynolds number flow past two and three circular cylinders using unstructured grid CFR scheme. *International Journal of Heat and Fluid Flow*, 31(2), 154–171. <https://doi.org/10.1016/j.ijheatfluidflow.2010.01.007>
- Hey, R. D., & Thorne, C. R. (1986). Stable channels with mobile gravel beds. *Journal of Hydraulic Engineering*, 112(8), 671–689. [https://doi.org/10.1061/\(asce\)0733-9429\(1986\)112:8\(671\)](https://doi.org/10.1061/(asce)0733-9429(1986)112:8(671))
- Igarashi, T., & Suzuki, K. (1984). Characteristics of the flow around three circular cylinders arranged in line. *SME International Journal Series C Mechanical Systems, Machine Elements and Manufacturing*, 27(233), 2397–2404. <https://doi.org/10.1299/jsme1958.27.2397>
- Jalalabadi, R., Stoesser, T., Ouro, P., Luo, Q., & Xie, Z. (2021). Free surface flow over square bars at different Reynolds numbers. *Journal of Hydro-Environment Research*, 36, 67–76. <https://doi.org/10.1016/j.jher.2021.03.005>
- Julien, P. (1995). *Erosion and sedimentation*. Cambridge University Press.
- Kara, S., Kara, M. C., Stoesser, T., & Sturm, T. W. (2015). Free-surface versus rigid-lid LES computations for bridge-abutment flow. *Journal of Hydraulic Engineering*, 141(9), 04015019. [https://doi.org/10.1061/\(asce\)hy.1943-7900.0001028](https://doi.org/10.1061/(asce)hy.1943-7900.0001028)
- Lagasse, P., Zevenberger, L., & Clopper, P. (2010). Impacts of debris on bridge pier scour. In *Scour and Erosion, International Conference on Scour and Erosion*. American Society of Civil Engineers.
- Lane, S. (2017). Natural flood management. *Wiley Interdisciplinary Reviews: Water*, 4(3), e1211. <https://doi.org/10.1002/wat2.1211>
- Liu, Y., Stoesser, T., Fang, H., Papanicolaou, A., & Tsakiris, A. G. (2017). Turbulent flow over an array of boulders placed on a rough, permeable bed. *Computers & Fluids*, 158, 120–132. <https://doi.org/10.1016/j.compfluid.2017.05.023>
- Luo, Q., Dolcetti, G., Stoesser, T., & Tait, S. (2023). Water surface response to turbulent flow over a backward-facing step. *Journal of Fluid Mechanics*, 966, A18. <https://doi.org/10.1017/jfm.2023.350>

- McSherry, R., Chua, K., Stoesser, T., & Mulahasan, S. (2018). Free surface flow over square bars at intermediate relative submergence. *Journal of Hydraulic Research*, 56(6), 825–843. <https://doi.org/10.1080/00221686.2017.1413601>
- Meneghini, J. R., Saltara, F., Siqueira, C. D. L. R., & Ferrari, J., Jr. (2001). Numerical simulation of flow interference between two circular cylinders in tandem and side-by-side arrangements. *Journal of Fluids and Structures*, 15(2), 327–350. <https://doi.org/10.1006/jfls.2000.0343>
- Moballa, B., Chern, M.-J., & Borthwick, A. (2020). Incompressible SPH simulation of flow past horizontal cylinder between plane wall and free surface. *Journal of Fluids and Structures*, 97, 103091. <https://doi.org/10.1016/j.jfluidstructs.2020.103091>
- Muhawenimana, V., Follett, E., Maddock, I., & Wilson, C. A. M. E. (2023). Field-based monitoring of instream leaky barrier backwater and storage during storm events. *Journal of Hydrology*, 1, 129744. <https://doi.org/10.1016/j.jhydro.2023.129744>
- Muhawenimana, V., Wilson, C. A., Nefjodova, J., & Cable, J. (2021). Flood attenuation hydraulics of channel-spanning leaky barriers. *Journal of Hydrology*, 596, 125731. <https://doi.org/10.1016/j.jhydro.2020.125731>
- Müller, S., Follett, E. M., Ouro, P., & Wilson, C. (2022). Influence of channel-spanning engineered logjam structures on channel hydrodynamics. *Water Resources Research*, 58(12), e2022WR032111. <https://doi.org/10.1029/2022wr032111>
- Müller, S., Wilson, C. A., Ouro, P., & Cable, J. (2021a). Experimental investigation of physical leaky barrier design implications on Juvenile Rainbow Trout (*Oncorhynchus mykiss*) movement. *Water Resources Research*, 57(8), 1–17. <https://doi.org/10.1029/2021wr030111>
- Müller, S., Wilson, C. A., Ouro, P., & Cable, J. (2021b). Leaky barriers: Leaky enough for fish to pass? *Royal Society Open Science*, 8(3), 201843. <https://doi.org/10.1098/rsos.201843>
- Nicoud, F., & Ducros, F. (1999). Subgrid-scale stress modelling based on the square of the velocity. *Flow, Turbulence and Combustion*, 62(3), 183–200. <https://doi.org/10.1023/a:1009995426001>
- Nikora, V. I., Stoesser, T., Cameron, S. M., Stewart, M., Papadopoulos, K., Ouro, P., et al. (2019). Friction factor decomposition for rough-wall flows: Theoretical background and application to open-channel flows. *Journal of Fluid Mechanics*, 872, 626–664. <https://doi.org/10.1017/jfm.2019.344>
- Nisbet, T., Roe, P., Marrington, S., Thomas, H., Broadmeadow, S., & Valatin, G. (2015). *Defra FCERM multi-objective flood management demonstration project, Project RMP5455: Slowing the flow at Pickering, final report: Phase II* (Tech. Rep.). Department for Environment.
- Osher, S., & Sethian, J. A. (1988). Fronts propagating with curvature-dependent speed: Algorithms based on Hamilton-Jacobi formulations. *Journal of Computational Physics*, 79(1), 12–49. [https://doi.org/10.1016/0021-9991\(88\)90002-2](https://doi.org/10.1016/0021-9991(88)90002-2)
- Ouro, P., Fraga, B., Lopez-Novoa, U., & Stoesser, T. (2019). Scalability of an Eulerian-Lagrangian large-eddy simulation solver with hybrid MPI/OpenMP parallelisation. *Computers & Fluids*, 179, 123–136. <https://doi.org/10.1016/j.compfluid.2018.10.013>
- Ouro, P., Lopez-Novoa, U., & Guest, M. F. (2021). On the performance of a highly-scalable Computational Fluid Dynamics code on AMD, ARM and Intel processor-based HPC systems. *Computer Physics Communications*, 269, 108105. <https://doi.org/10.1016/j.cpc.2021.108105>
- Ouro, P., Mullings, H., Christou, A., Draycott, S., & Stallard, T. (2024). Wake characteristics behind a tidal turbine with surface waves in turbulent flow analysed with large-eddy simulation. *Physical Review Fluids*, 9, 34608.
- Ouro, P., & Nishino, T. (2021). Performance and wake characteristics of tidal turbines in an infinitely large array. *Journal of Fluid Mechanics*, 925, A30. <https://doi.org/10.1017/jfm.2021.692>
- Papaioannou, G. V., Yue, D. K. P., Triantafyllou, M. S., & Karniadakis, G. E. (2006). Three-dimensionality effects in flow around two tandem cylinders. *Journal of Fluid Mechanics*, 558, 387–413. <https://doi.org/10.1017/s0022112006000139>
- Pitt, M. (2008). Learning lessons from the 2007 floods. *Pitt Review*.
- Pugh, C. A. (2008). Sediment transport scaling for physical models. In *Sedimentation engineering: Processes, measurements, modeling, and practice* (pp. 1057–1065).
- Reich, M. (2003). Restoring streams with large wood: A synthesis. In *The ecology and management of wood in world rivers*.
- Reichl, P., Hourigan, K., & Thompson, M. (2003). The unsteady wake of a circular cylinder near a free surface. *Flow, Turbulence and Combustion*, 71(1–4), 347–359. <https://doi.org/10.1023/b:appl.0000014926.99751.b1>
- Reichl, P., Hourigan, K., & Thompson, M. (2005). Flow past a cylinder close to a free surface. *Journal of Fluid Mechanics*, 533, 269–296. <https://doi.org/10.1017/s0022112005004209>
- Schalcko, I., Lageder, C., Schmocker, L., Weitbrecht, V., & Boes, R. (2019). Laboratory flume experiments on the formation of spanwise large wood accumulations: Part II—Effect on local scour. *Water Resources Research*, 55(6), 4871–4885. <https://doi.org/10.1029/2019wr024789>
- Sheridan, J., Lin, J., & Rockwell, D. (1995). Metastable states of a cylinder wake adjacent to a free surface. *Physics of Fluids*, 7(9), 2099–2101. <https://doi.org/10.1063/1.868458>
- Sheridan, J., Lin, J., & Rockwell, D. (1997). Flow past a cylinder close to a free surface. *Journal of Fluid Mechanics*, 330, 1–30. <https://doi.org/10.1017/s002211209600328x>
- Shields, A. (1936). *Anwendung der aehnlichkeitsmechanik und der turbulenzforschung* PhD Thesis (Vol. 26). Technical University.
- Shvidchenko, A. B., & Pender, G. (2000). Flume study of the effect of relative depth on the incipient motion of coarse uniform sediments. *Water Resources Research*, 36(2), 619–628. <https://doi.org/10.1029/1999wr900312>
- Stoesser, T. (2014). Large-eddy simulation in hydraulics: Quo Vadis? *Journal of Hydraulic Research*, 52(4), 441–452. <https://doi.org/10.1080/00221686.2014.944227>
- Sumner, D. (2010). Two circular cylinders in cross-flow: A review. *Journal of Fluids and Structures*, 26(6), 849–899. <https://doi.org/10.1016/j.jfluidstructs.2010.07.001>
- Sussman, M., Smereka, P., & Osher, S. (1994). A level set approach for computing solutions to incompressible two-phase flow. *Journal of Computational Physics*, 114(1), 146–159. <https://doi.org/10.1006/jcph.1994.1155>
- Tong, F., Cheng, L., & Zhao, M. (2015). Numerical simulations of steady flow past two cylinders in staggered arrangements. *Journal of Fluid Mechanics*, 765, 114–149. <https://doi.org/10.1017/jfm.2014.708>
- Uhlmann, M. (2005). An immersed boundary method with direct forcing for the simulation of particulate flows. *Journal of Computational Physics*, 209(2), 448–476. <https://doi.org/10.1016/j.jcp.2005.03.017>
- Wang, X., & Tan, S. (2007). Experimental investigation of the interaction between a plane wall jet and a parallel offset jet. *Experiments in Fluids*, 42(4), 551–562. <https://doi.org/10.1007/s00348-007-0263-9>
- Wohl, E. (2013). Floodplains and wood. *Earth-Science Reviews*, 123, 194–212. <https://doi.org/10.1016/j.earscirev.2013.04.009>
- Wohl, E., & Iskin, E. P. (2022). The transience of channel-spanning logjams in mountain streams. *Water Resources Research*, 58(5), e2021WR031556. <https://doi.org/10.1029/2021wr031556>
- Wohl, E., & Jaeger, K. (2009). A conceptual model for the longitudinal distribution of wood in mountain streams. *Earth Surface Processes and Landforms*, 34(3), 329–344. <https://doi.org/10.1002/esp.1722>
- Wu, S., & Rajaratnam, N. (1995). Free jumps, submerged jumps, and wall jets. *Journal of Hydraulic Research*, 33(2), 197–212. <https://doi.org/10.1080/00221689509498670>

- Yokoi, K. (2013). A practical numerical framework for free surface flows based on CLSVOF method, multi-moment methods and density-scaled CSF model: Numerical simulations of droplet splashing. *Journal of Computational Physics*, 232(1), 252–271. <https://doi.org/10.1016/j.jcp.2012.08.034>
- Yokoi, K., Onishi, R., Deng, X. L., & Sussman, M. (2016). Density-scaled balanced continuum surface force model with a level set based curvature interpolation technique. *International Journal of Computational Methods*, 13(04), 1–20. <https://doi.org/10.1142/s0219876216410048>
- Zdravkovich, M. (1977). Review of flow interference between two circular cylinders in various arrangements. *Journal of Fluids Engineering*, 99(4), 618–633. <https://doi.org/10.1115/1.3448871>
- Zhang, N., Rutherford, I., & Ghisalberti, M. (2020). Effect of instream logs on bank erosion potential: A flume study with a single log. *Journal of Ecohydraulics*, 5(1), 43–56. <https://doi.org/10.1080/24705357.2019.1634499>